NASA CONTRACTOR REPORT

NASA CR-629

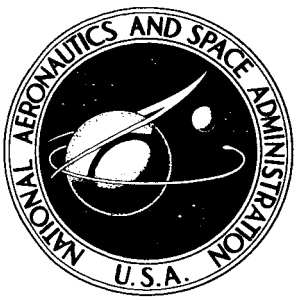

NASA CR-629

RESEARCH PROGRAM ON PYROELECTRIC DETECTION TECHNIQUES AND MATERIALS

PHASE II

Prepared by
SPERRY RAND CORPORATION
Clearwater, Fla.
for

NATIONAL AERONAUTICS AND SPACE ADMINISTRATION • WASHINGTON, D. C. • DECEMBER 1966

NASA CR-629

RESEARCH PROGRAM ON PYROELECTRIC DETECTION TECHNIQUES AND MATERIALS

PHASE II

Prepared under Contract No. NASw-974 by
SPERRY RAND CORPORATION
Clearwater, Fla.

for

NATIONAL AERONAUTICS AND SPACE ADMINISTRATION

For sale by the Clearinghouse for Federal Scientific and Technical Information
Springfield, Virginia 22151 – Price $2.50

TABLE OF CONTENTS

LIST OF ILLUSTRATIONS

LIST OF ILLUSTRATIONS (cont.)

LIST OF ILLUSTRATIONS (cont.)

1. PURPOSE OF PROGRAM

The purpose of this program is to determine and demonstrate the basic features of pyroelectric radiation detectors. The goals of this, the second phase of the three-phase research program, are -

- To achieve a specific detectivity of 3×10^{8} cps $^{1/2}$ cm/watt,
- To evaluate the feasibility of making detectors with thin film active elements, and
- To arrive at detectors of utility in research being done by NASA at their Langley Research Center.

2. ABSTRACT

Several different materials were tested in an effort to determine materials with strong pyroelectric response. A figure of merit was defined by which one could combine measureable parameters of materials to determine their potential as detectors. These parameters were measured for several different materials. The result was that barium titanate and tri-glycine sulfate proved to have the most potential as detectors.

A single crystalline thin film effort was initiated in an effort to obtain thin film single crystals of high quality for detectors. This was initiated because theory predicts the specific detectivity to be proportional to the inverse square root of thickness. Etching techniques were pursued for the same reasons.

Hot spots were observed and studied. Details are included in this report.

The Langley effort led to a strong concentration toward ceramic detectors. These were tested in the Hot Shot Tunnel at Langley Research Center. Results of tests are included herein as are details.

The theory of the pyroelectric effect was reviewed and changes were made for application to ceramic materials.

3. PUBLICATIONS, LECTURES, REPORTS, CONFERENCES AND TRIPS

3.1 PUBLICATIONS

None in this reporting period.

3.2 LECTURES

None in this reporting period.

3.3 REPORTS

None in this reporting period.

3.4 CONFERENCES

None in this reporting period.

3.5 TRIPS

Tests were held at the Hot Shot Tunnel facility at Langley Research Center from August 23 to 27. In attendance were Mr. Pierce Lawing and Mr. Cary Spitzer of Langley Research Center and Mr. Travis G. Hickman of Sperry Microwave Electronics Company. Five shots were conducted to determine the agreement between the ceramic pyroelectric detectors and thermocouples, both of which were installed in the model. The trip was considered very successful.

4. RESULTS OF WORK PERFORMED DURING THIS INTERVAL

4.1 INTRODUCTION

The following is a final report on Contract No. NASw-974 summarizing the results of the previous quarterly reports and analyzing the scope of the entire program. This includes a search for materials of higher quality and measuring their various parameters in order to determine their potential as detectors. To this end, a figure of merit was found which depended on measurable parameters and which would indicate the potential of a material. A single crystalline thin film effort was in the program as was an extensive effort in etching, both of which came about because the theory predicted a higher specific detectivity for thinner detectors. Polycrystalline ceramic detectors were investigated and tested in the Hot Shot Tunnel at Langley Research Center. The theory was then re-examined in an effort to modify it for polycrystalline materials.

In Section 4.2, the results of the testing of various pyroelectric crystals will be covered with photographs of their hysteresis loops.

In Section 4.3, a figure of merit is discussed, which made it possible to predict the pyroelectric potential of a material by examining its parameters. Measurement of these parameters and the equipment used in these measurements are discussed in detail.

Single crystalline thin films are discussed in Section 4.4 and the various methods of growth considered are discussed in detail. X-ray diffraction patterns are included as are evaluations of the films grown. Thin film work was initiated as a result of theoretical indications that thinner crystals would yield higher specific detectivities. In line with these indications, etching techniques were used to obtain thinner single crystals. These techniques are discussed in Section 4.5.

Section 4.6 discusses the phenomenon of hot spots, how they were observed, and possible causes.

The polycrystalline detectors constructed for testing in the Hot Shot Tunnel at Langley Research Center are discussed in Section 4.7. This includes their fabrication mounting, calibration and testing; and a summary of the effort.

Section 4.8 contains results of measurements as a function of thickness to be followed by a theoretical discussion in Section 4.9.

4.2 TESTING OF NEW CRYSTALS

Several ferroelectrics were examined to find materials with an impressive pyroelectric response. To date, no materials have been found which approach the performance of TGS (tri-glycine sulfate) or $BaTiO_3$ (barium titanate.) The results

of measurements as to sensitivity of several previously untried ferroelectric materials are given in Table I.

TABLE I

Single Crystal	NEP in watt/$(cps)^{\frac{1}{2}}$
$LiNbO_3$	4×10^{-6}
$(CH_2NH_2COOH)_3 \cdot H_2BeF_4$	2×10^{-6}
$NaNO_2$	Had discernible response but NEP unmeasurable
$Pb(NbFe)O_3$	No response
$PbBi_2Nb_2O_9$	No response
$K(V_{.5}Nb_{.5})O_3$	No response
$Na(V_{.1}Nb_{.9})O_3$	No response

Two independent set of measurements were made and each set yielded the same results. Capacitance measurements and hysteresis loops were made on the last five detectors in an effort to determine if faulty electrodes might have been the reason for not getting a pyroelectric response. The capacitances measured were somewhat low but were reasonable figures. Figures 1, 2, 3, and 4 are hysteresis loops from detectors 3, 5, 6 and 7, respectively. Detector 4 cracked before a loop could be made. While there is no evidence to indicate that bad electrodes were the reason for not getting a response from these detectors, it should be noted that the detectors were very small and irregular and such could have been the case.

Crystals received from NASA Headquarters are as follows:

$SrTiO_3$

$BaTiO_3$

$Eu_2O_3 \cdot TiO_2$ (prepared under several different conditions)

Results of tests run on these crystals failed to reveal anything promising. Samples of the barium titanate furnished gave a pyroelectric signal and showed a specific detectivity of $1.2 \times 10^4 (cps)^{\frac{1}{2}}$ cm/watt. By comparison, locally fabricated ceramic detectors of barium titanate have given specific detectivities as high as $3.8 \times 10^6 (cps)^{\frac{1}{2}}$ cm/watt and locally grown barium titnate crystals have shown specific detectivities as high $1.1 \times 10^7 (cps)^{\frac{1}{2}}$ cm/watt. As a further comparison, the hysteresis

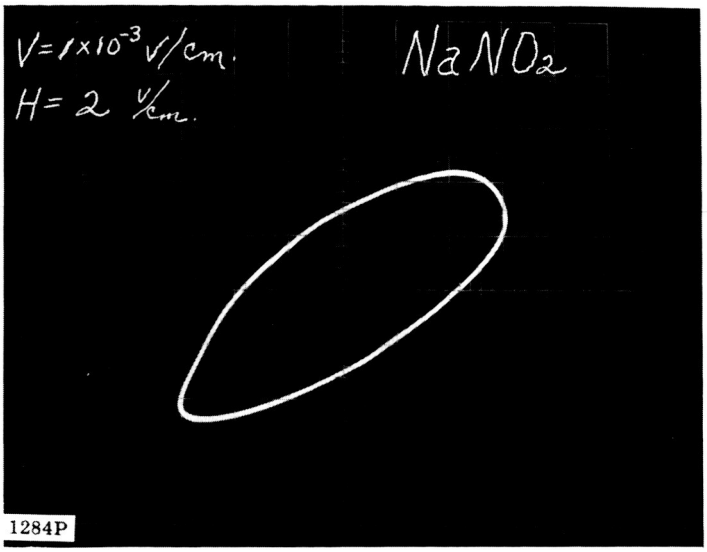

Figure 1. Hysteresis Loop from $NaNO_2$ Single Crystal

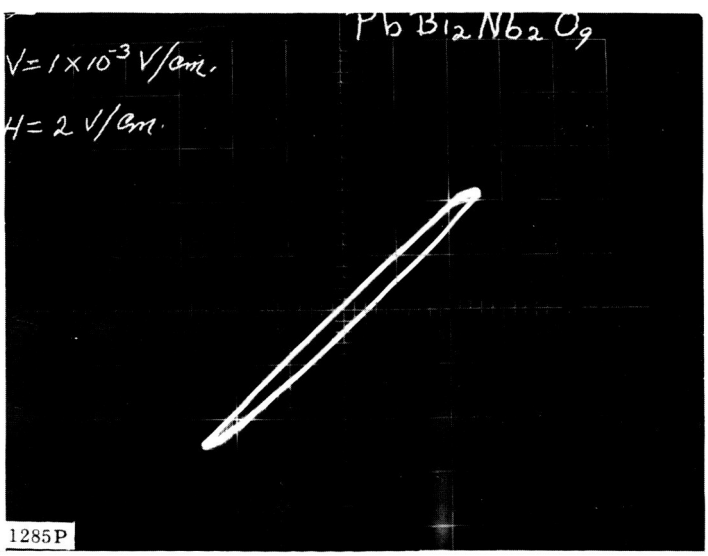

Figure 2. Hysteresis Loop from $PbBi_2Nb_2O_9$ Single Crystal

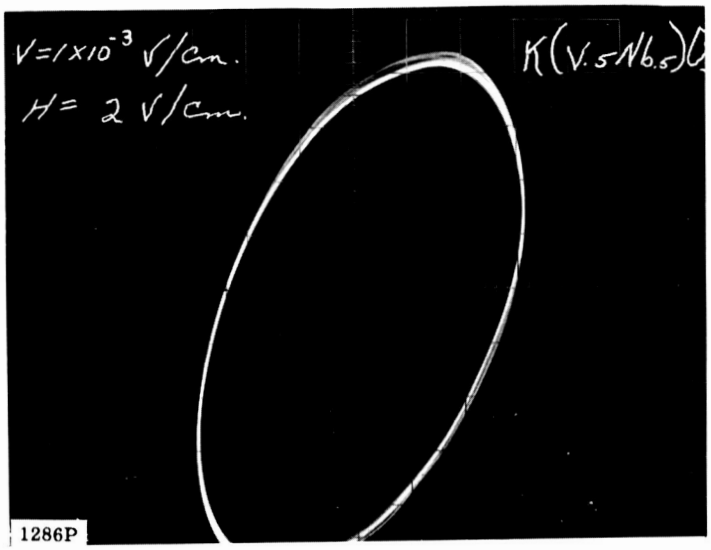

Figure 3. Hysteresis Loop from $K(V_{.5}Nb_{.5})O_3$ Single Crystal

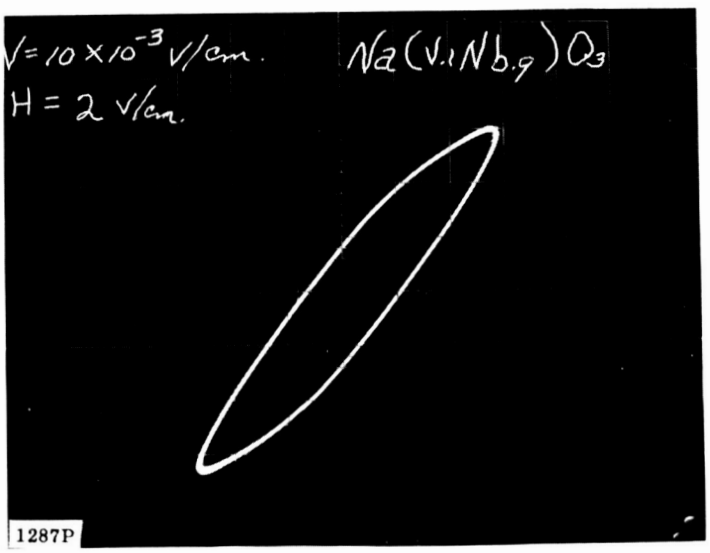

Figure 4. Hysteresis Loop from $Na(V_{.1}Nb_{.9})O_3$ Single Crystal

loop shown in Figure 5 from the crystal being tested can be compared with the loop shown in Figure 6 from a typical locally grown barium titanate crystal. While P_r is much higher ffor the cyrstal in Figure 6 than the one in Figure 5, the differences in amplification are somewhat deceiving.

None of the other crystals from NASA gave a pyroelectric signal. Only one other crystal gave a hysteresis loop. This loop is shown in Figure 7. Though not very impressive, this loop was given by the $Eu_2O_3 \cdot 2TiO_2$ crystal shown in Figure 8. To indicate the size of the electroded crystal, a human hair is shown at the top of the photograph. No other crystals exhibited pyroelectric properties.

4.3 FIGURE OF MERIT

It is shown in Section 4.9 that a reasonable figure of merit for pyroelectric material is

$$F = (dP_S/dT)/c_p \rho \sqrt{\epsilon' \tan \delta}$$

Thus the larger F is for a given material, the better it should be as a pyroelectric detector. Consequently, the potential of a given material can be determined by measuring the parameters comprising F.

This information was not available on many of the crystals to be examined, so it was necessary to devise means of making measurements of the indicated parameters. The sections that follow will describe these measurements and the devices which had to be constructed for these measurements.

4.3.1 Specific Heat Measurements

The lack of data on the specific heats of various crystals led to the construction of a calorimeter (Figure 9) from block styrofoam. This material was selected for its convenience and extremely low heat conductance. The calorimeter was designed for very small samples and satisfactory measurements were made on crystals weighing as little as 0.1 gram. A copper constantan thermocouple was used to measure the temperature change of the methyl alcohol. The methyl alcohol was selected for its low heat capacity and inactivity with various ferroelectric crystals.

To achieve measurable quantities, a temperature change on the order of 30°C was required. Since c_p is generally dependent upon temperature, the c_p measured was an average value over this temperature. However, values obtained were good indications as to the expected quality of detector the crystal will make.

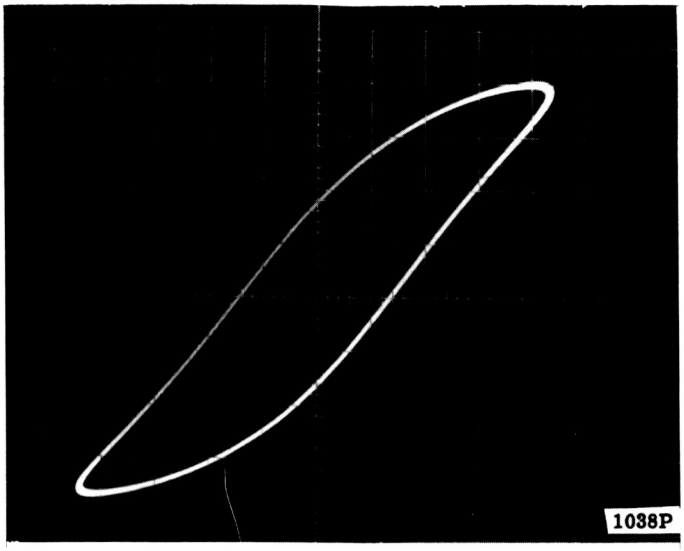

Figure 5. Hysteresis Loop from Barium Titanate Crystal Received from R. R. Nash at NASA Headquarters for Examination and Possible Use in Pyroelectric Program. The Horizontal Axis Gives the Polarizing Field in Relative Units. The Vertical Axis Gives the Polarization in Relative Units.

Figure 6. Hysteresis Loop from Barium Titanate Crystal Grown at Sperry Microwave Electronics Company. The Horizontal Axis Gives the Polarizing Field in Relative Units. The Vertical Axis Gives the Polarization in Relative Units.

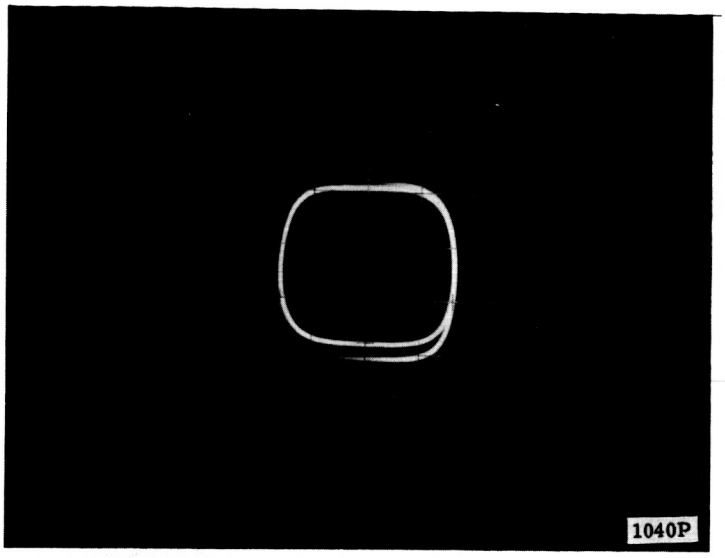

Figure 7. Hysteresis Loop from $Eu_2O_3 . 2TiO_2$ Crystal Received from R. R. Nash for Examination and Possible Use in Pyroelectric Program. The Horizontal Axis gives the Polarizing Field in Relative Units. The Vertical Axis Gives the Polarization in Relative Units.

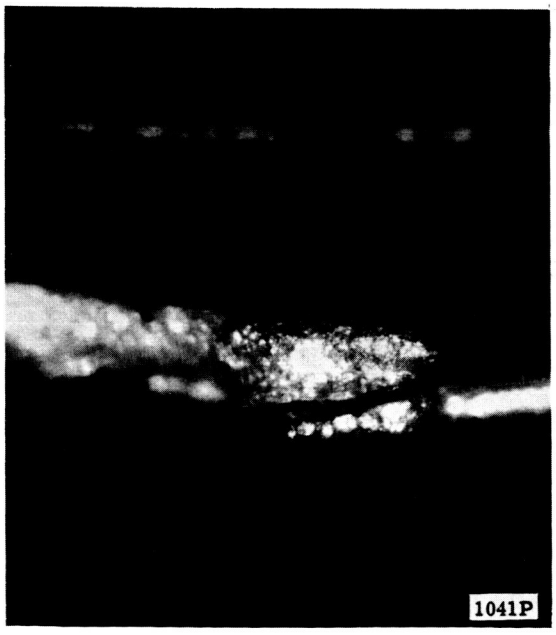

Figure 8. $Eu_2O_3 . 2TiO_2$ Crystal with Electrodes. This Crystal Gave the Hysteresis Loop Shown in Figure 7. The Object Above the Crystal is a Human Hair.

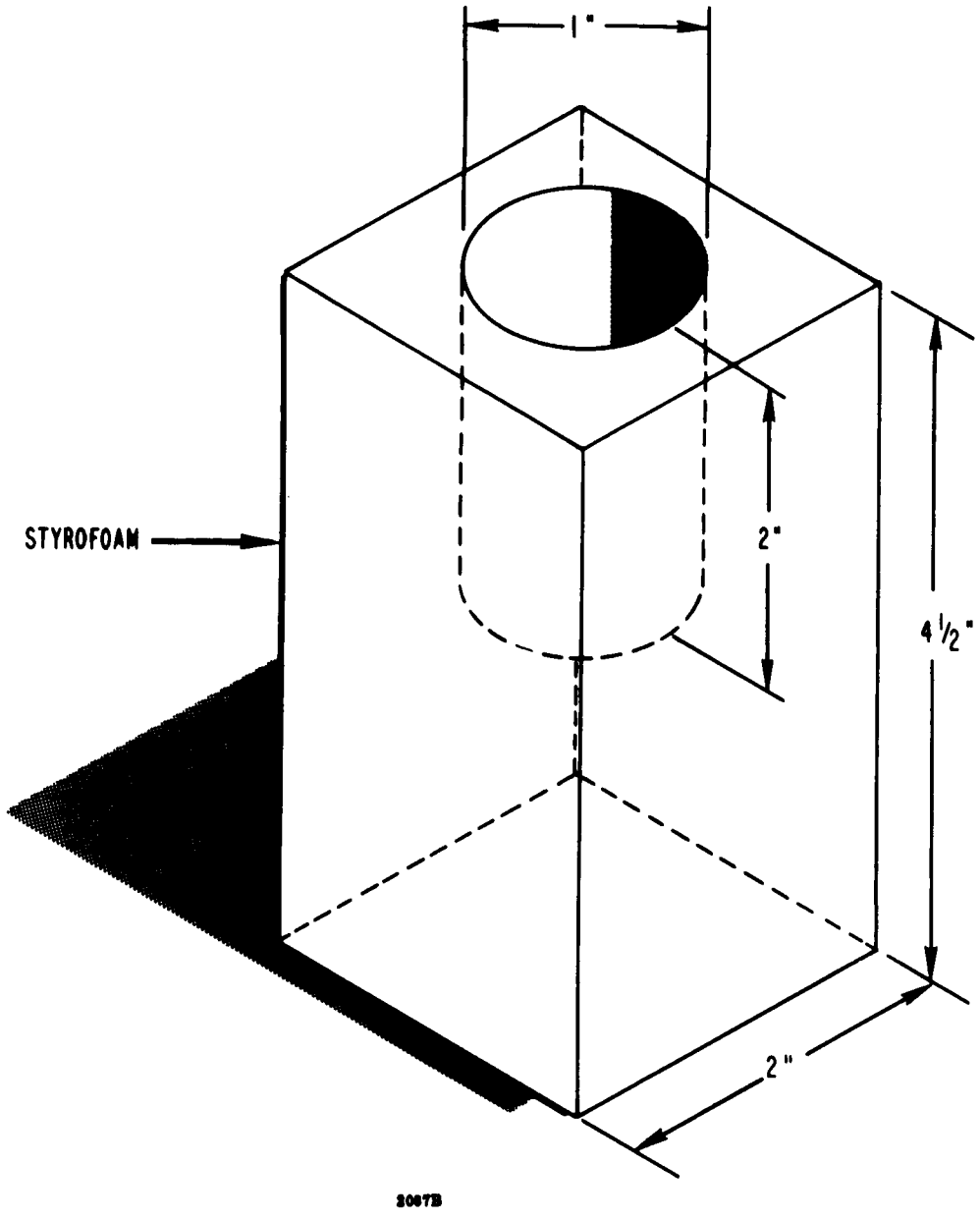

Figure 9. Calorimeter

Measurements were made on materials with known specific heats as a check on the reliability of the calorimeter. The results were satisfactory. For example, two consecutive runs on TGS gave specific heats of 78.5 cal/mole^{o}C and 80.1 cal/mole^{o}C. These values agree well with the curve[1] for specific heat vs temperature for TGS as shown in Figure 10. A list of specific heat measurements made with this calorimeter is given below.

Crystal	Specific Heat (Cal./gm. ^{o}C)
$(NH_2CH_2COOH)_3 \cdot H_2BeF_4$ (Triglycine Fluoberyllate)	0.367
L_1NbO_3	0.180
$(NH_2CH_2COOH)_3 \cdot H_2SO_4$ (Triglycine Sulfate)	0.246
$B_2T_1O_3$	0.121
$C(NH_2)_3\ Al(SO_4)_2 \cdot 6H_2O$	0.218

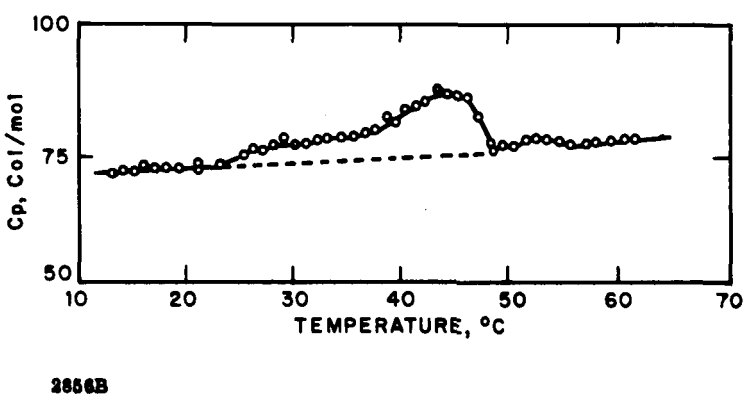

Figure 10 Specific Heat of Tri-Glycine Sulfate as a Function of Temperature

[1] Jona, Franco, and Shirane, G., Ferroelectric Crystals, p. 38.

4.3.2 Pyroelectric Coefficient and Dielectric Constant

It should be noted at this time that while it is popular to give the pyroelectric coefficient as $\frac{dP_s}{dT}$ in publications, the actual pyroelectric coefficient is $\frac{dP_r}{dT}$ where P_r is the remanent polarization or that polarization which actually remains when the polarizing field has been removed. However, the difference in the two values is so small that it can be neglected and the pyroelectric coefficient is commonly written as $\frac{dP_s}{dT}$.

A circuit to measure the spontaneous polarization of a detector was made. The change in spontaneous polarization with respect to temperature, $\frac{dP_s}{dT}$, is the pyroelectric coefficient. Evaluation of measurements made with this cirucit, however, showed the slope of the linear portion, A, of the hysteresis loop in Figure 11 to be too large, causing the dielectric constant to be too large. Excessive terminal capacitance was the source of this error. Changing connectors lowered this capacitance to a level where the circuit could function satisfactorily A test run on a $BaTiO_3$ single crystal gave the results depicted in Figures 12 and 13.

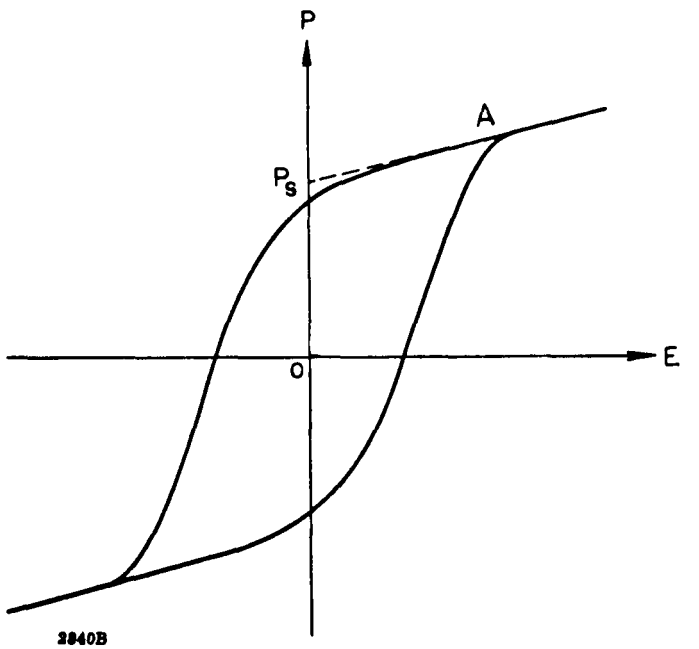

Figure 11. Hysteresis Loop of a Typical Ferroelectric Material Showing the Spontaneous Polarization P_s Obtained by Extrapolating the Linear Portion A of the Curve to the E = 0 Axis.

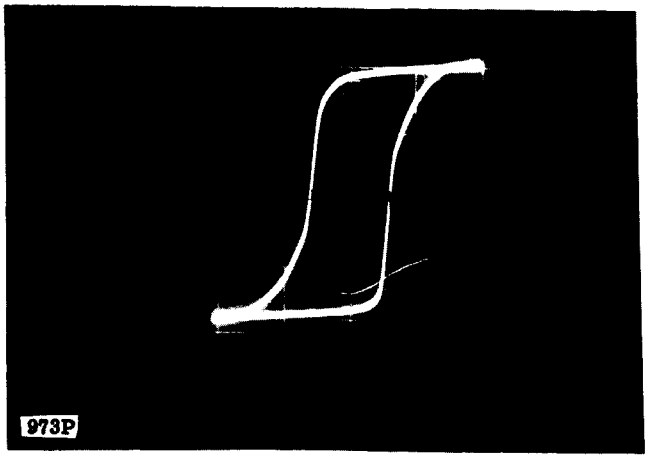

Figure 12. Hysteresis Loop of a Single Crystal of $BaTiO_3$ Used to Determine Spontaneous Polarization P_s

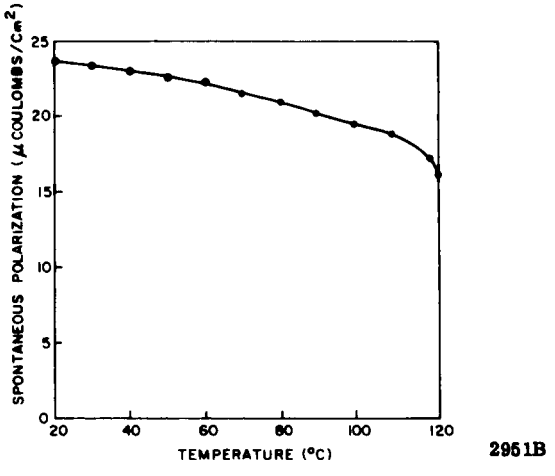

Figure 13. Spontaneous Polarization vs Temperature for $BaTiO_3$

When all the dipoles in a ferroelectric are aligned, the material behaves as any linear dielectric; therefore, the slope of the hysteresis loop in the linear portion at the extremes is a measure of the dielectric constant of the material.

A linear material whose slope goes through the origin obeys the equation $D = \epsilon E$. We therefore define the quantity P_s (spontaneous polarization) as the additive term which would move the line from one passing through the origin to one which is coincident with the linear portion, A, of the hysteresis loop in Figure 11. Therefore $D = \epsilon E + P_s$ in this linear portion of the curve. The slope of this line therefore is

$$\frac{dD}{dE} = \epsilon = \epsilon_o \epsilon_r,$$

where ϵ_0 is the permittivity of free space and ϵ_r is the dielectric constant.

It should be noted that ϵ is measured in the saturation region of the loop where the ferroelectric behaves as a dielectric. This is not the ϵ given by the equation

$$\epsilon = \lim_{E \to 0} \frac{dD}{dE} \text{ but is instead}$$

$$\epsilon = \epsilon_0 \epsilon_r = \left.\frac{dD}{dE}\right| \text{ saturated}$$

for the ferroelectric. The circuit used to measure the spontaneous polarization is given in Figure 14.

From Gauss' law, $D = \frac{Q}{A_x}$, where Q is the charge on the crystal and A_x is its area. Therefore, $D = \frac{CV_v}{A_x}$, since the charge Q is the same on each capacitor. Since $C_x \ll C$, is approximately given by

$$E = \frac{V}{\ell} = \frac{(R_1 + R_2)V_h}{R_2}$$

where ℓ is the thickness of the crystal. Therefore

$$\epsilon_r = \frac{1}{\epsilon_0} \frac{dD}{de}$$

$$= \frac{R_2 \ell C}{\epsilon_0 (R_1 + R_2) A_x} \frac{dV_v}{dV_h}$$

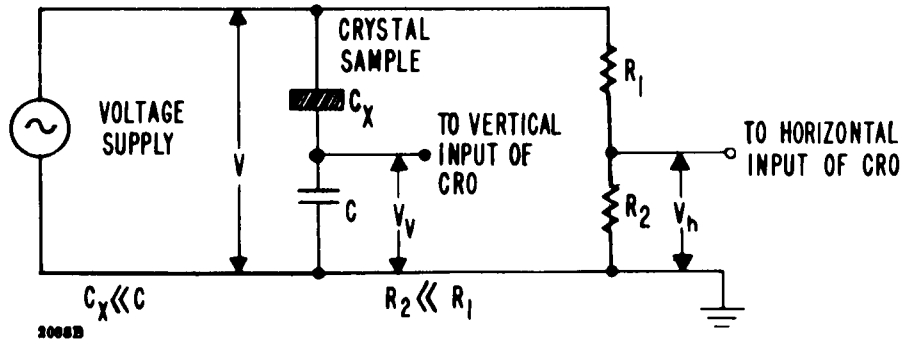

Figure 14. Circuit Used to Measure Spontaneous Polarization

Since $R_1 \gg R_2$, ϵ_r can be approximately expressed as

$$\epsilon_r = \frac{R_2 \ell C}{\epsilon_o R_1 A_x} \frac{dV_v}{dV_h}$$

and the error resulting from this approximation is less than the error resulting from reading the slope of the line from the oscilloscope.

The dielectric constant for tri-glycine sulfate was found to be 52.4 at 26°C using this circuit. This was closer than could be read from the graphs in the literature. Using the same crystal, the spontaneous polarization was measured as a function of temperature. The resulting curve (Figure 15) is in good agreement with curves in the literature[2].

Typical hysteresis loops for tri-glycine sulfate and barium titanate are shown in Figures 16 and 17 respectively.

4.3.3 Loss Tangent

A circuit similar to the one in Figure 14 was also used to measure loss tangents of various materials. If the voltage level of the generator is set to a low level and the crystal is not saturated, the voltages to both the horizontal and vertical plates of the cathode ray oscilloscope will be sinusoidal but will differ by a phase angle. This will be discussed in detail in the theoretical section following later in the report and the equations will be derived. If the amplification at the oscilloscope is adjusted until the amplitudes of both these voltages are the same, an ellipse is observed whose semimajor axis is oriented at 45° to the horizontal axis. This angle is constant regardless of the loss tangent. However, the ratio of the semiminor axis to the semimajor axis varies with the loss tangent which is given by:

$$\tan \delta = \frac{2\frac{b}{a}}{1-\left(\frac{b}{a}\right)^2},$$

where b is the semiminor axis and a is the semimajor axis. Using this device, we were able to measure loss tangents at the chopping frequencies. Loss tangents given in the literature are usually measured at microwave frequencies and do not shed much light on behavior of the crystals at the low frequency chopping rate.

[2] Jona, Franco, and Shirane, G., Ferroelectric Crystals, p 31.

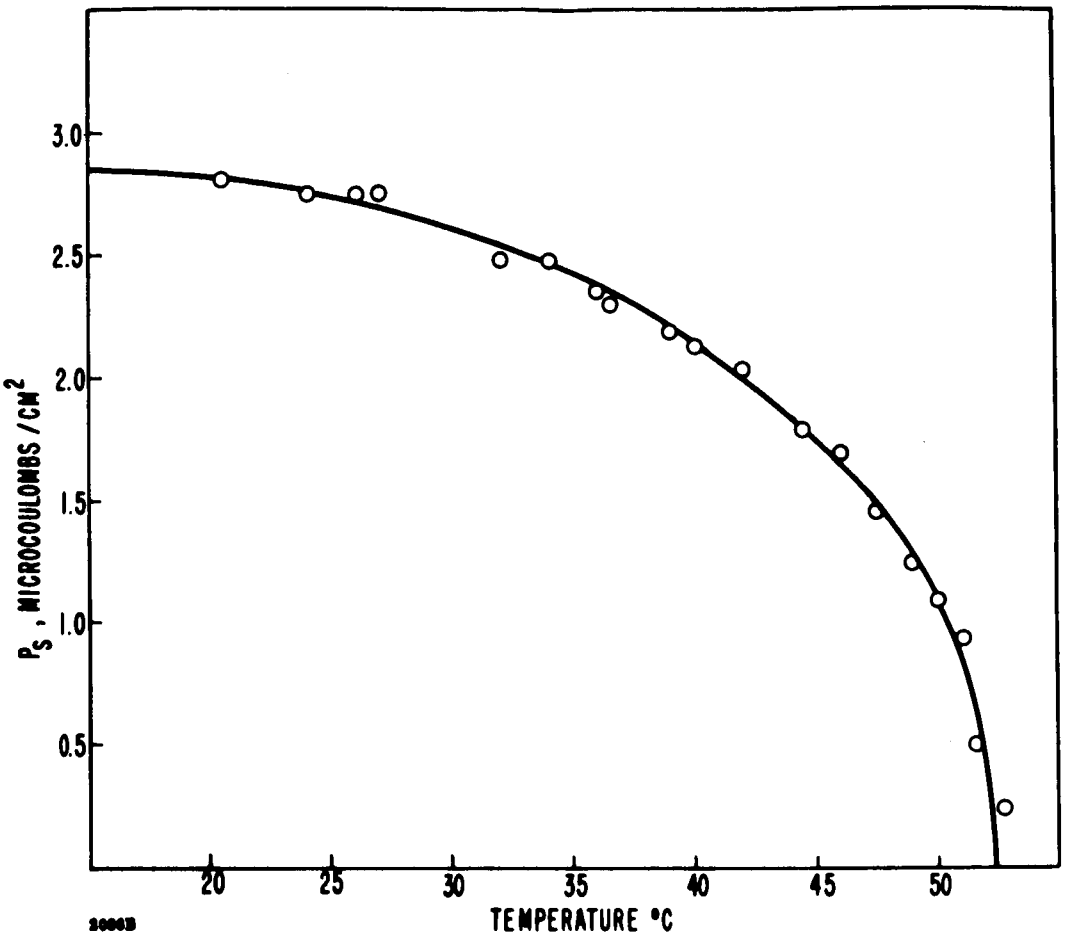

Figure 15. Spontaneous Polarization of Tri-Glycine Sulfate as a Function of Temperature as Measured with Circuit Shown in Figure 14.

4.4 SINGLE CRYSTALLINE THIN FILMS

The goal of this activity was to grow thin-film single crystals of ferroelectric materials suitably oriented for incorporation into pyroelectric detectors. The general approach being utilized was that featuring epitaxial growth of the ferroelectric material onto a suitable substrate.

Once a thin film had been obtained, its characterization could be conveniently divided into two distinct steps. First, it had to be verified that the thin film was in fact ferroelectric. Second, it was desired to establish whether or not it was a single crystal. The details of this effort are given below.

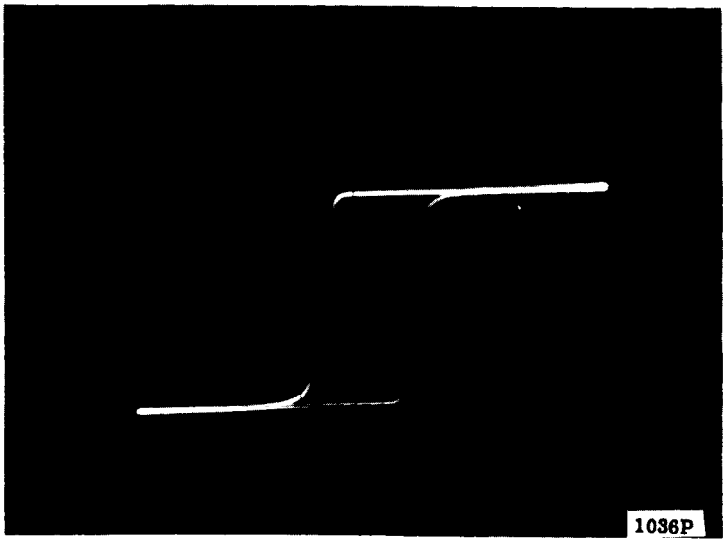

Figure 16. Hysteresis Loop from Tri-Glycine Sulfate Detector. The Horizontal Axis Gives the Polarizing Field in Relative Units. The Vertical Axis Gives the Polarization in Relative Units.

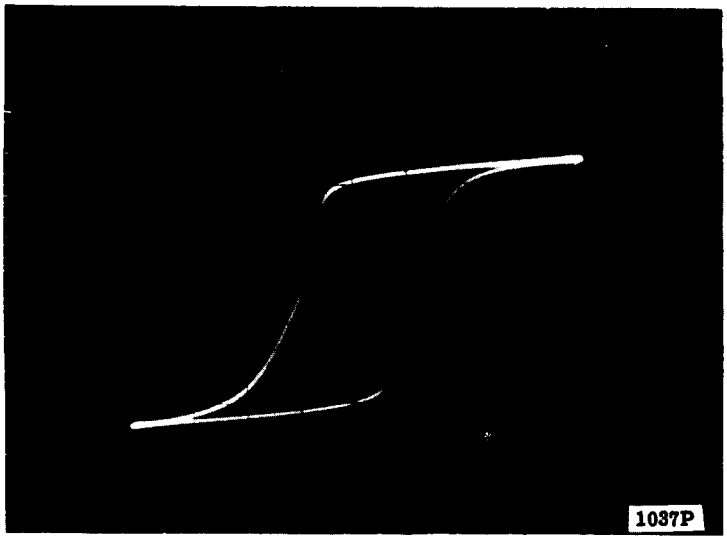

Figure 17. Hysteresis Loop from Barium Titanate Detector. The Horizontal Axis Gives the Polarizing Field in Relative Units. The Vertical Axis Gives the Polarization in Relative Units.

4.4.1 General Approach

Based on a literature survey, the procedure was to base all attempts to achieve thin-film single crystals of ferroelectrics on the preferred orientation of thin-films obtained by epitaxial deposition onto a suitable single crystalline substrate. Techniques available for obtaining such epitaxial growth vary somewhat with the material being deposited. Inasmuch as no pyroelectric materials had been found which approached the performance of TGS (triglycine sulfate) or $BaTiO_3$ (barium titnate) as detector elements, only these materials were included in the thin film investigations.

Techniques of deposition considered were:

- Evaporation of Saturated Solutions, and
- Vapor Depositions

The technique involving evaporation of saturated solutions was considered for both TGS and $BaTiO_3$.

1. Surface Tension Method: In this method, a single crystal substrate (or a polycrystalline substrate having large single crystalline areas) is partially submerged edgewise into a saturated solution of the ferroelectric material. The solution is then allowed to wet the substrate for some distance above the surface of the solution. As the solution wetting the substrate evaporates, the ferroelectric material is deposited onto the substrate[3].

2. Solution Interface Contact: This method consists of wetting an appropriate face of a pyroelectric single crystal with a solvent and placing it momentarily face down onto a suitable single crystalline substrate material. As the solvent evaporates, a thin film is left on the substrate and hopefully will be oriented. This technique may be particularly useful for TGS, which is water soluble.

3. Liquid Drop Evaporation: This technique consists of placing a drop of saturated solution onto a single crystalline substrate and allowing it to evaporate. This technique differs from (2) only in the manner of "wetting" the substrate.

The vapor deposition technique was considered for $BaTiO_3$ only.

1. Component Evaporation: This method involves the evaporation of BaO from one filament and the evaporation of TiO_2 from a second. These materials are collected onto the same substrate and subsequently heat treated to yield $BaTiO_3$. Again, the single crystalline substrate will hopefully provide preferred orientation.

---

[3] See for example, R.C. DeVries, "On the Preparation of Thin Single Crystal Films of $BaTiO_3$, J. Am. Ceramic Soc. 45, 225(1962).

2. Flash Evaporation: This method involves rapid evaporation of small single crystals of $BaTiO_3$ onto a single crystalline substrate. The rapid evaporation allows the evaporated crystal to disassociate into $BaTiO_3$ molecules instead of decomposing into BaO and TiO_2 molecules, as is normal.

3. Phase Melting: DeVries[4] suggested that one might obtain thin film single crystals of $BaTiO_3$ by very quickly raising the temperature so that it is above the "extrapolated" melting point for the cubic phase, but below the actual melting point. Thus, the cubic phase might melt before it has time to change phase. The melted portion would "run-out" onto the substrate and recrystallize into its proper phase for the higher temperature.

Since the thin film single crystals were attempted to provide sensitive detecting elements, electrodes had to be placed on each side of the film. Due to the fragility of the film and complications encountered in the removal of this film from a substrate, the provision of electrode was not a trivial problem. It was decided to first grow a thin-film single crystal of a good electrical conductor and then deposit the thin single crystal of the ferroelectric on top of the conductor. This would make the removal of the thin film from its substrate unnecessary.

4.4.2 Gold Thin Film Work

Due to the electrode problem mentioned above, the first project undertaken was to grow gold thin-film single crystals. This was accomplished by using a single crystal of NaCl as a substrate and evaporating gold onto it. The mount used to hold the substrate in the vacuum chamber and the vacuum heater constructed to control the temperature of the substrate are pictured in Figure 18.

The overall procedure was as follows:

1. The vacuum chamber housing the NaCl crystal and gold was evacuated to approximately 8 millimicrons of Hg.
2. The crystal was then heated to 140°C and held for 2 hours.
3. The temperature was then increased and stabilized at 270°C.
4. Gold was then evaporated onto the crystal at the rate of 100 Å/minute. A gold wire 1.0 inch long and 0.040 inch diameter was evaporated over a period of 40 minutes.
5. Temperature of the NaCl substrate was reduced to 200°C and held for 30 minutes.

[4] R. C. DeVries, private communication.

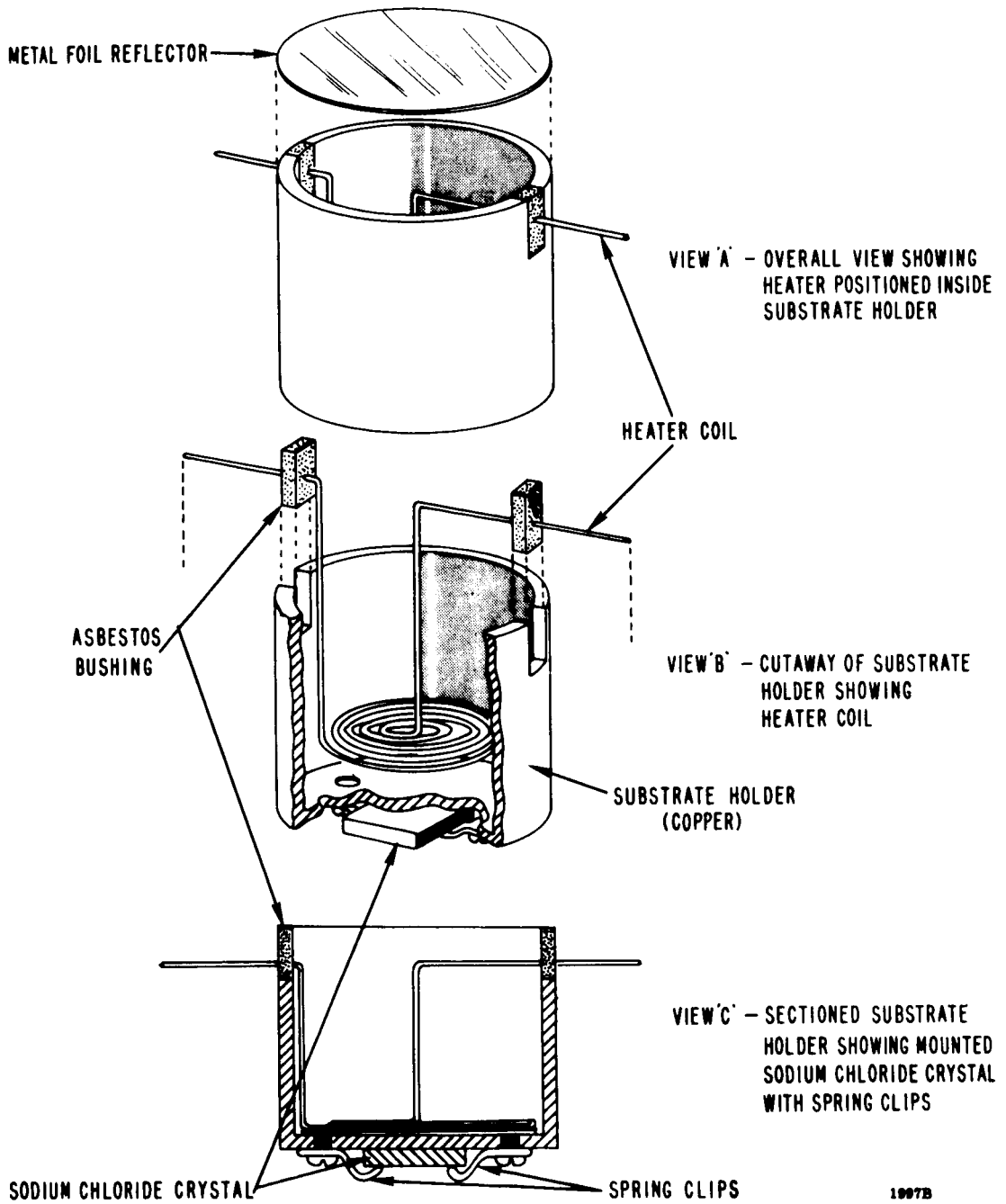

Figure 18. Substrate Holder and Heater for Deposition of Gold by Evaporation

6. Substrate heater was turned off and substrate was allowed to cool for 30 minutes (it cooled to 65°C) before being removed from the vacuum.

The film was checked for its single crystalline nature by dissolving the sodium chloride away from the gold film, putting the latter on a glass slide and then taking an x-ray Laue pattern of the film. The result is shown in Figure 19. As can be seen from the figure, the thin film is predominately single crystalline. The strong asterism present in the Laue pattern is felt to be due to crystal strain.

4.4.3 TGS Thin-Film Work

A gold film prepared as outlined in Section 4.5.2 was placed partially submerged with its face approximately normal to the surface of the solution. After remaining in this configuration for one week, a thin film of TGS was noted on the gold film. Attempts to ascertain if the film was primarily single crystalline by X-ray Laue patterns were not definitive.

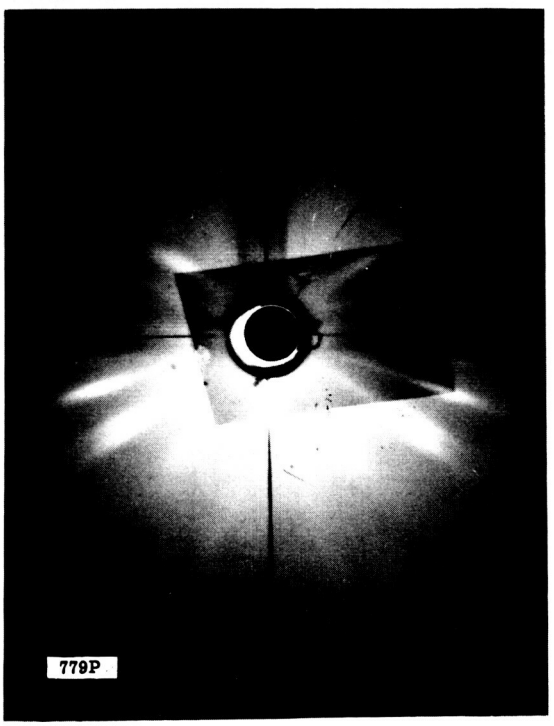

Figure 19. Laue Pattern for Thin Film Gold (4000A°) Deposited by Evaporation onto Single Crystalline Substrate of NaCl

The thin film was electroded and checked for hysteresis and the resulting plot of electric displacement versus electric field is shown in Figure 20. The circuit used to obtain this plot is given in Figure 21.

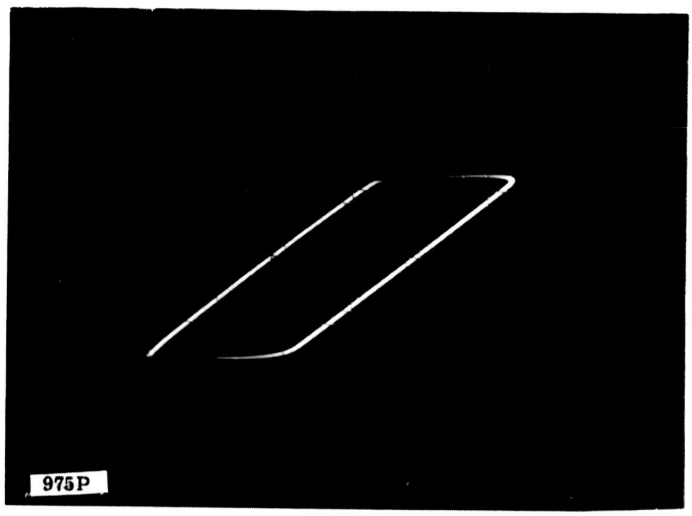

Figure 20. Hysteresis Loop for TGS Thin Film

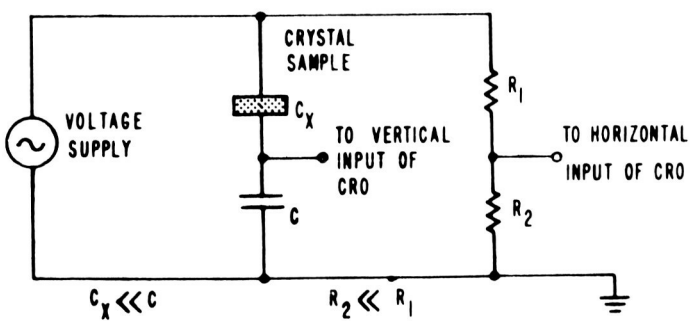

Figure 21. Circuit Used to Measure Spontaneous Polarization

The hysteresis observed and depicted in Figure 20 suggests that the film is ferroelectric. However, all attempts to polarize the film and observe the pyroelectric signal failed. During the latter measurements the film shorted out. To date, no pyroelectric signal has been observed using thin films grown by the above techniques.

4.4.4 $BaTiO_3$ Thin Film

The first attempts to grow single crystalline thin films of the $BaTiO_3$ were based on a method used by John P. Green at MIT[5]. In this process, layers of BaO are alternated with layers of TiO_2 onto a platinum substrate. Simultaneous evaporation of BaO and TiO_2 onto the substrate was also carried out. The resulting films were then heated to 1150°C, held at that temperature for 6 hours and then allowed to cool. Films prepared in this manner did not exhibit hysteresis and a new technique was tried.

The second attempt to obtain thin film single crystals of $BaTiO_3$ was based on the work of Müller et al.[6] Briefly, this attempt consists of the following procedure. $BaTiO_3$ crystals are crushed to small particle sizes ranging from 150 microns to 250 microns. These are then "flash" evaporated onto a single crystalline substrate of LiF by allowing the grains of $BaTiO_3$ to fall individually onto an iridium boat heated resistively to about 2200°C. The main problem here is getting electrodes on both sides without destroying the sample.

Because of the electrode problem, a thin film single crystal of gold on NaCl substrate was used as a substrate for the "flash" evaporation of $BaTiO_3$. A gold electrode was then evaporated onto the front and the resulting sample checked for hysteresis. The resulting loop is shown in Figure 22. It should be noted that the single crystalline gold substrate was highly strained.

Five samples of thin film gold were carefully deposited on single crystalline NaCl in a final attempt to achieve single crystalline substrates for $BaTiO_3$ films. These films were examined with the electron microscope at the General Electric facility in St. Petersburg. A strong degree of single crystallinity was observed in two of the films.

[5] John P. Green, Jr., "A Method for Fabricating Thin Ferroelectric Films of Barium Titanate", Tech. Memo. ESL-TM-105, Electronic Systems Laboratory, MIT, Cambridge 39, Massachusetts, April 1961.

[6] E. K. Müller, B. J. Nicholson, and G. L'E. Turner, "The Epitaxial Vapor Deposition of Perovskite Materials", Journal of the Electromechanical Society, 110, 969 (September, 1963).

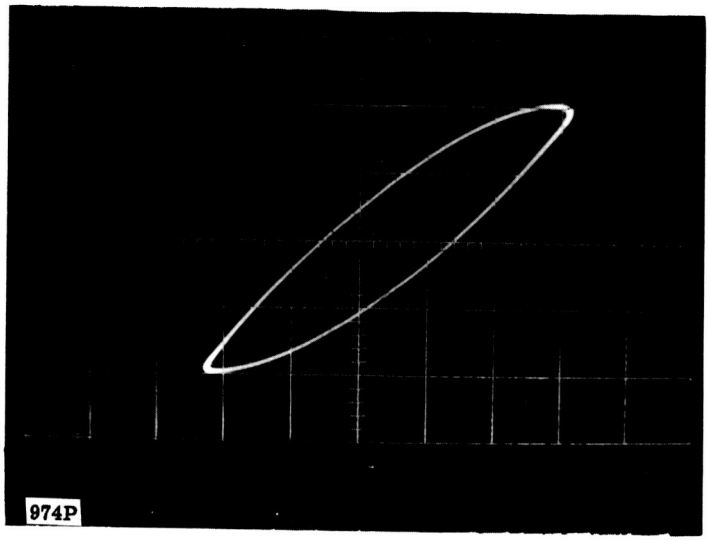

Figure 22. Hysteresis Loop for Thin Film $BaTiO_3$ Deposited Onto Highly Strained, Single Crystalline, Thin Film Gold

Figure 23 shows the pattern taken from one of these samples. An X-ray diffraction pattern indicated that growth was in the 100 plane. These films were used as substrates for epitaxial growth of $BaTiO_3$.

Barium titanate was flash evaporated onto this gold film by sprinkling it onto an iridium boat at 2200°C. This very fast evaporation allows the crystal to disassociate into $BaTiO_3$ molecules instead of decomposing into molecules of BaO and TiO_2. Difficulty was encountered with the iridium boat, since iridium melts at 2450°C and apparently was softening at the operating temperature. The boats tended to burn out before completion of the evaporation in about three of every four runs and the system had to be shutdown to replace this filament.

Examination of these barium titanate films which were approximately 500°A thick showed that they too were single crystalline. A pressed contact was put on the other side of the crystal and a hysteresis loop was observed. This loop, shown in Figure 24, gave hope of attaining an extremely high specific detectivity, however this was not the case. In fact, no pyroelectric signal could be detected at all. Because of these unfavorable developments, little hope is given to the chances of acheiving successful thin film single crystal detectors without a major effort in this area.

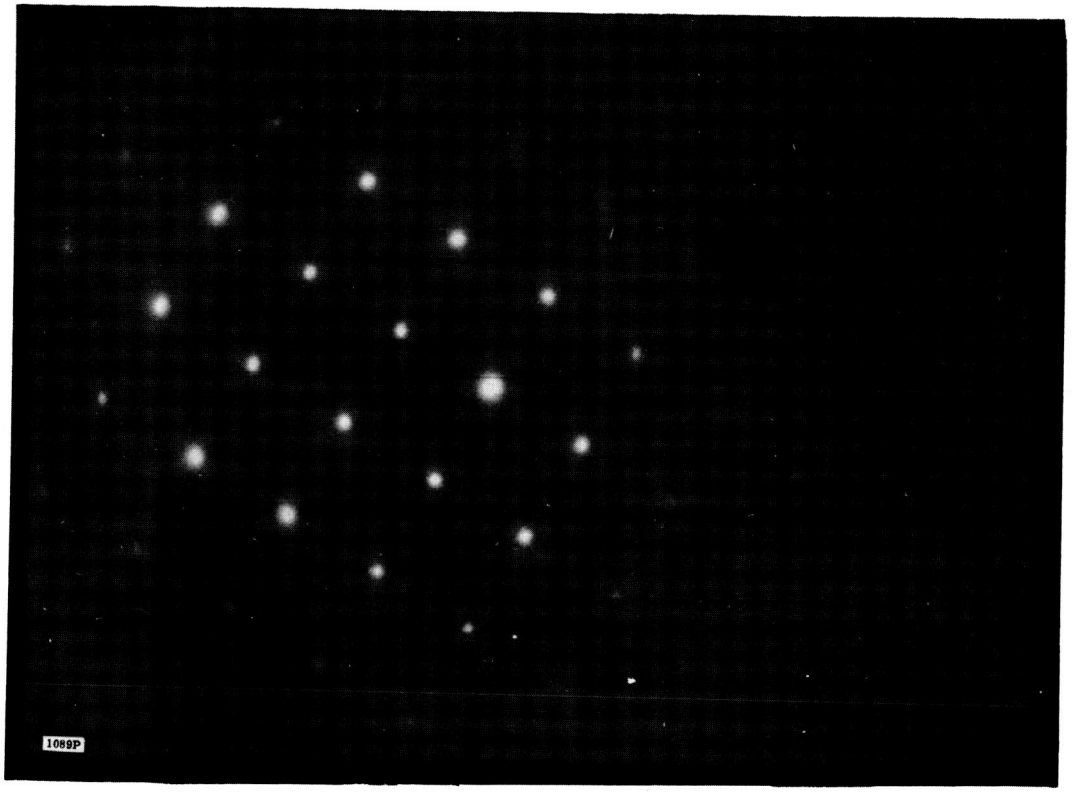

Figure 23. Diffraction Pattern of Single Crystal Gold Film Epitaxially Deposited on a Single Crystal of Sodium Chloride. The Pattern was Taken with the Electron Microscope at the General Electric Facility at St. Petersburg, Florida.

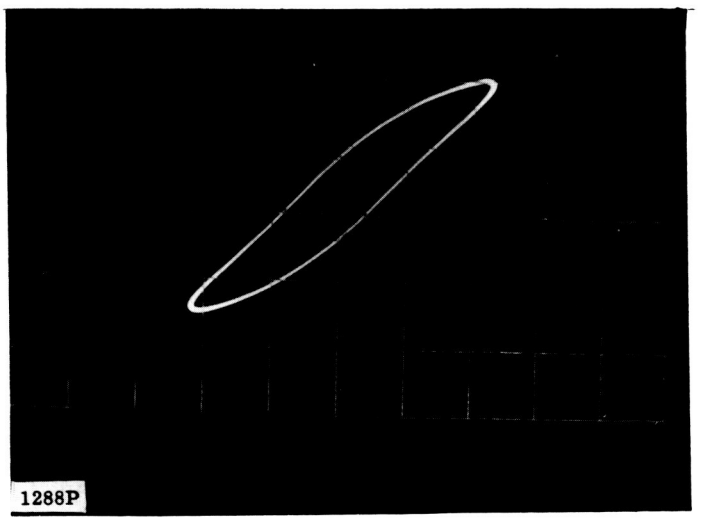

Figure 24. Hysteresis Loop from Thin Film Single Crystal of Barium Titanate. The Horizontal Axis Gives the Polarizing Field in Relative Units. The Vertical Axis Gives the Polarization in Relative Units.

4.5 ETCHING TECHNIQUES

For the region in which equation (1) is valid, it is seen that the NEP is directly proportional to the square root of the thickness of the detector. Herein lies the reason for desiring thinner detectors of good quality. Barium titanate crystals were successfully etched to a thickness of one mil, but beyond that, the surfaces became noticeably pitted or cracked and the response of the detector degenerated rapidly. While it was not possible to experimentally correlate specific detectivity with detector thickness due to other uncontrollable parameters, it is worthwhile to note that our best detectors of each material are 2 mils or less in thickness.

The etching was done in phosphoric acid above the Curie temperature of the crystal. Below the Curie temperature, the crystals are polarized and if all the dipoles are not aligned, the etching process will be nonuniform. The positive ends of the dipoles etch faster than the negative ends with the sides somewhere in between.[7] Therefore to insure uniform etching, it was done in the unpolarized state. These efforts failed to produce any detectors thinner than one mil.

As described in an article by Last[8] thin single crystals of $BaTiO_3$ were then mounted between two pieces of teflon tape, (3M No. 60), with windows cut in the tape for the areas to be etched (see Figure 25.) This was then put into phosphoric acid at 130°C and etched. According to the article, the etching should take place at a rate of about one micron per minute. The etching proceeded as described but the crystals tended to crack badly when they became thinner than one mil. The tape flexed badly and with crystals as thin as those in question, this would destroy the crystal.

A thin sheet of metal was shaped into a reinforcing perimeter in an attempt to prevent this flexing and thereby keep cracking to a minimum. However, attempts of this nature met with little success. While there was no noticeable flexing of the mask, the crystals still cracked badly.

Crystals were etched as thin as five microns but were badly cracked and failed to give any impressive results. Deposition of electrodes on these crystals tended to make the cracks worse, probably because of the thermal shock accompanying the vaporization of aluminum. Indium was deposited on the crystals, since the melting point of indium is extremely low (157°C). The cracking did not increase during this deposition, indicating that the thermal shock probably was cracking the crystals, but

[7] Hooten, J.A. and Merz, W.J. Phys. Rev. 98, 409(1955).

[8] J.T. Last, Rev. Sci. Inst. 28, 720 (September, 1957).

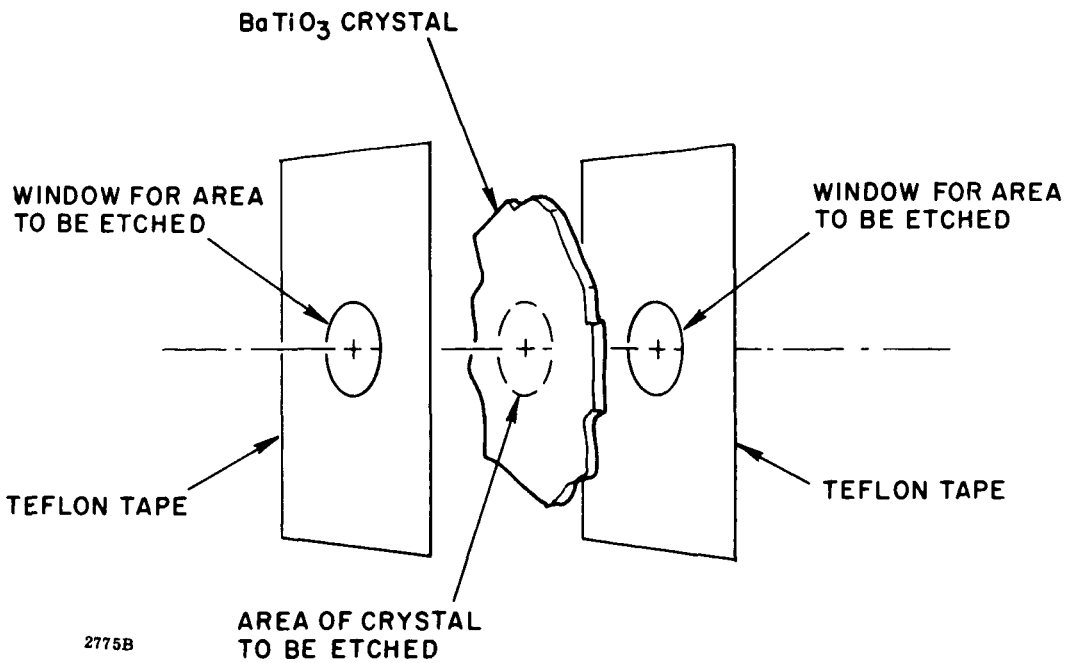

Figure 25. Diagram of Mask which is Used In Etching Process Showing Crystal In Place.

indium did not deposit evenly. The electrodes thus deposited were not suitable for detectors because the indium tended to gather in splotches instead of depositing evenly.

Tri-glycine sulfate crystals have given higher specific detectivities than have barium titanate thus far, yielding specific detectivities as high as 1.2×10^8 $(cps)^{1/2}$ cm/watt for thinner samples. They are cleaved to a thickness of approximately 10 mils, then etched as far as possible. Being water soluble, these crystals are more convenient to work with than barium titanate; however, they are also influenced by humidity and tend to deteriorate with storage.

For example, a particular crystal was tested for sensitivity and found to have an NEP of 2.5×10^{-9} watts/$(cps)^{1/2}$. The crystal was then stored for for five months and tested again. Without repoling, the crystal had an NEP of 1.0×10^{-7} watts/$(cps)^{1/2}$. Repoling the crystal did not improve its response. The efficiency of the crystal, therefore was down by a factor of 50 after five months storage.

Efforts to obtain thin single crystals of barium titanate have met with only limited success. While crystals have been etched as thin as 5 microns, cracking is a very serious problem, and few detectors survive this etching process intact. The 5 micron detector had a specific detectivity two orders of magnitude lower than our best one mil detector, and it is felt that poor electroding was largely responsible for this low figure.

4.6 HOT SPOTS

The phenomenon of hot spots was observed early in the research program. Later in the program, these observations were reconfirmed and these spots were studied. A helium neon gas laser was used in the following manner to study these spots. The laser beam was focused to a point and this point scanned the face of the crystal. A portion of the laser beam was reflected by a plate of glass and monitored to insure that it was not fluctuating in intensity. Hot spots were then observed on several different crystals. It was observed that areas of extremely high sensitivity, that is, up to 150 times the signal given by other areas of the crystal, occurred around the area of contact between the electrode and the lead wire. This contact was made with silver paint.

Figure 26 shows a blown-up photograph of one of the single crystal detectors of $BaTiO_3$ taken on a metallograph. In the lower portion of the photograph is a darkened area, A, in the shape of a circle. This area consists of two electrodes of evaporated aluminum, one on the front side of the crystal and one on the back. At the bottom of the photograph, notice the lead wire, B, which is attached to the front electrode by means of the silver paint which is the very dark area, C, covering roughly one-half of the electrode. The lead wire which is connected to the back electrode, is in the dark portion, D, at the top of the photograph. This is connected to the electrode by the narrow strip, E, which is a strip of evaporated aluminum. The entire area "C" is extremely hot on this particular crystal and in the center of this area the sensitivity is roughly 100 times the average sensitivity over the remaining portion of the crystal. The area shown by "F" on the figure is also hotter than the average for the electroded area. It is interesting to note that this particular area is not even on the electrode but around the edge.

The aluminum electrodes were removed from a crystal and replaced with silver ones thinking that perhaps the silver had something to do with the increased sensitivity. However, this did not show any improvement over the aluminum electrodes. Similar spots of increased sensitivity occurred around the edge of the electrodes but the effect was much smaller than around the lead wire. Here the effect was only about 10 times the sensitivity of the rest of the crystal.

Further inquiry into hot spots was prohibited due to the increased effort on the Langley work and a malfunction of the laser which occurred late in the program.

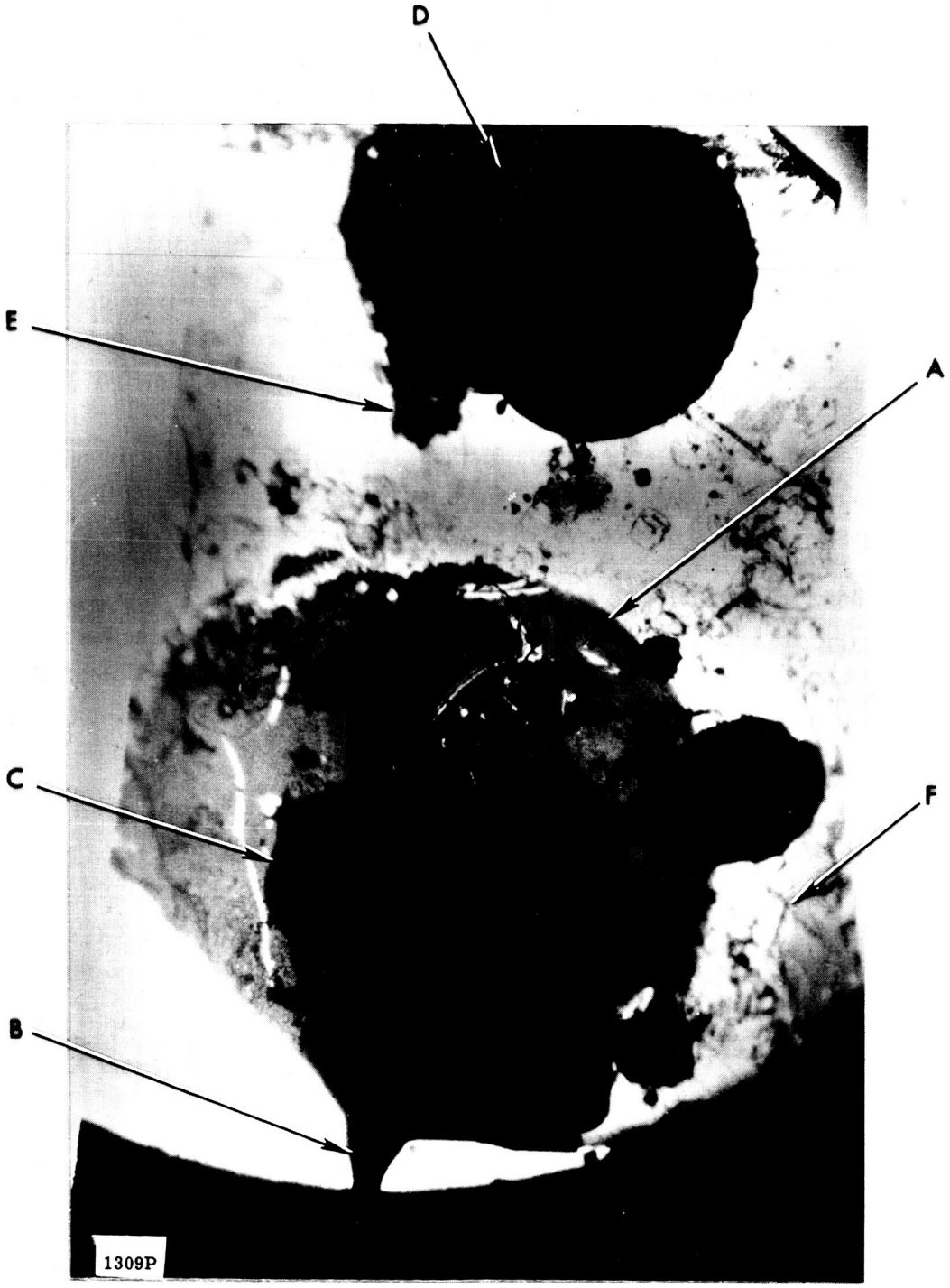

Figure 26. Single Crystal of Barium Titanate Showing Electrodes and Areas of High Pyroelectric Response

4.7 PREPARATION FOR HOT SHOT TUNNEL TESTS

4.7.1 Fabrication of Ceramic Detectors

The problem of preparing sufficiently thin ceramic detector elements was solved. The original approach to this problem was to first grind the detector elements to a thickness of 10 mils and then use lapping techniques to further reduce the thickness. This technique proved unfeasible due to cracking of the detector element during the lapping stage.

Considerable effort in achieving thin ceramic detectors free from cracks resulted in preparing them as follows. The elements were ground to a thickness of 7 mils with no lapping. This produced elements free of cracks and of sufficient sensitivity for the hot shot tunnel tests. Thinner samples which are free from cracks were achieved only with considerable additional effort. It was felt that this additional effort was unwarranted for the tests to be conducted in as much as intensities of the order of 100 watts/cm ^{2} would be encountered. Thus, only moderate sensitivity was required.

4.7.2 Reproducibility of Detector Response

Prior to mounting detector elements in the model provided by the Langley Research Center, four elements were prepared and measured under equivalent conditions. They were all circular in cross section with a diameter of 100 mils and a thickness of 7 mils. The NEP's measured for these samples are tabulated in Table II.

TABLE II *

DETECTOR	RESPONSIVITY (volts/watt)	NEP (watts/cps$^{1/2}$)
1	0.880	$1.42(10)^{-6}$
2	0.865	$1.44(10)^{-6}$
4	0.840	$1.47(10)^{-6}$
5	0.840	$1.47(10)^{-6}$

* Ceramic detector No. 3 was shorted out in attempting to pole it.

As can be seen from Table II, all NEP's were the same to within experimental error. The NEP's of the ten detectors mounted in the Langley model were not measured. However, their responsivity was measured and is given in Table III.

TABLE III

DETECTOR	AREA (cm^2)	RESPONSIVITY (volts/watt)
A	2.04×10^{-1}	0.131
B	5.1×10^{-2}	0.101
C	5.1×10^{-2}	0.118
D	5.1×10^{-2}	0.101
E	5.1×10^{-2}	0.101
F	5.1×10^{-2}	0.108
H	5.1×10^{-2}	0.145
J	5.1×10^{-2}	0.162
K	5.1×10^{-2}	0.148
L	5.1×10^{-2}	0.155

It is significant that preliminary results indicated that it was possible to achieve the same NEP from distinct ceramic detector elements constructed in the same manner. This was not possible using single crystals for the following reasons. First of all it is difficult to shape two crystals identically. If this shaping were achieved, differences in imperfections and strains prove sufficient to give rather large variations in response. Thus, comparisons of experimental results with theory have in the past been limited to a statistical nature. If it is assumed that the NEP of a single crystalline element (uniformly illuminated) deteriorates with crystalline strain and imperfections, it follows that only the best values should be compared with the theoretical model which assumes perfect polarization and cyrstal structure. This, in effect, is what has been done in the past and comparison of these best results with theory provided reasonable agreement.

However, the reproducibility exhibited by the ceramic elements suggested that a quantitative determination of NEP as a function of thickness could be made and the result compared with the theoretical dependence. One could start with several detectors having the same NEP and then determine their NEP as a function of thickness. In this way, any atypical elements could be discovered and ignored by making use of the reproducibility of elements. This investigation was carried out and will be summarized in a later section of the report.

4.7.3 Mounting of Detectors in Langley Model

Mounting detectors in the model proved difficult due to a 2 mil thick outer skin covering of stainless steel (see Figure 27). Any machining tended to separate this skin

from the model, regardless of how well it was clamped. Wooden forms were clamped to the model, and the holes to receive the detectors were drilled through both the wood and the model. This alleviated the separating problem somewhat but there was still a slight bulging around the holes. These holes were then tapped and nylon plugs were screwed as close to the surface as possible and still leave room for the detector element. For a cutaway drawing of the mounting, refer to Figure 27.

A nonconductive epoxy filled the space above the screw. The detector was then placed on the epoxy and adjusted to be flush with the surface. The epoxy was then allowed to harden. A closeup picture of one of the nylon screws mounted in the model is shown in Figure 28. Note the four circular holes where the thermocouples were later installed by Langley. The 2 mil stainless steel skin forms the bottom of these holes.

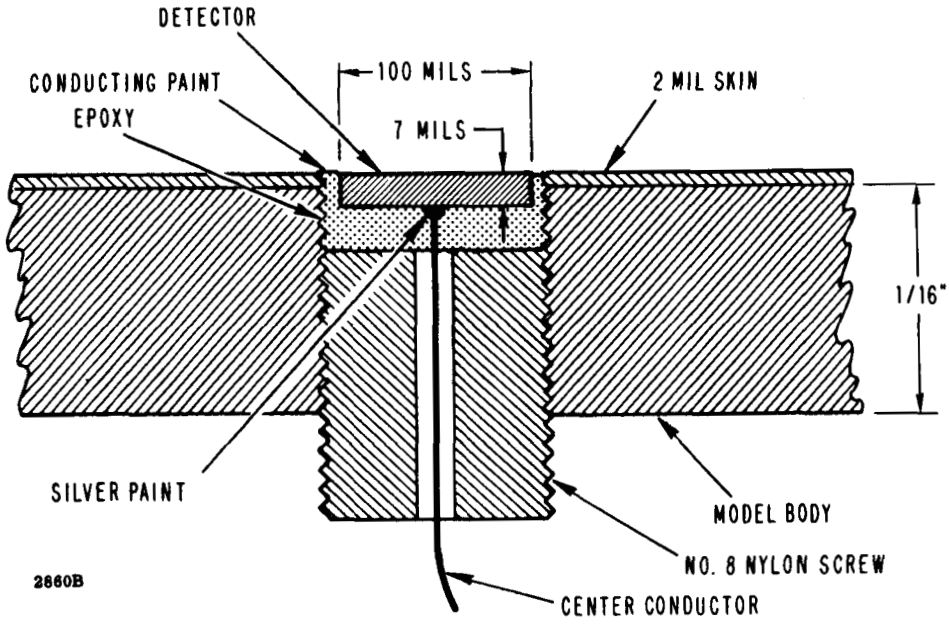

Figure 27. Cutaway Drawing of Detector Mounted in Model

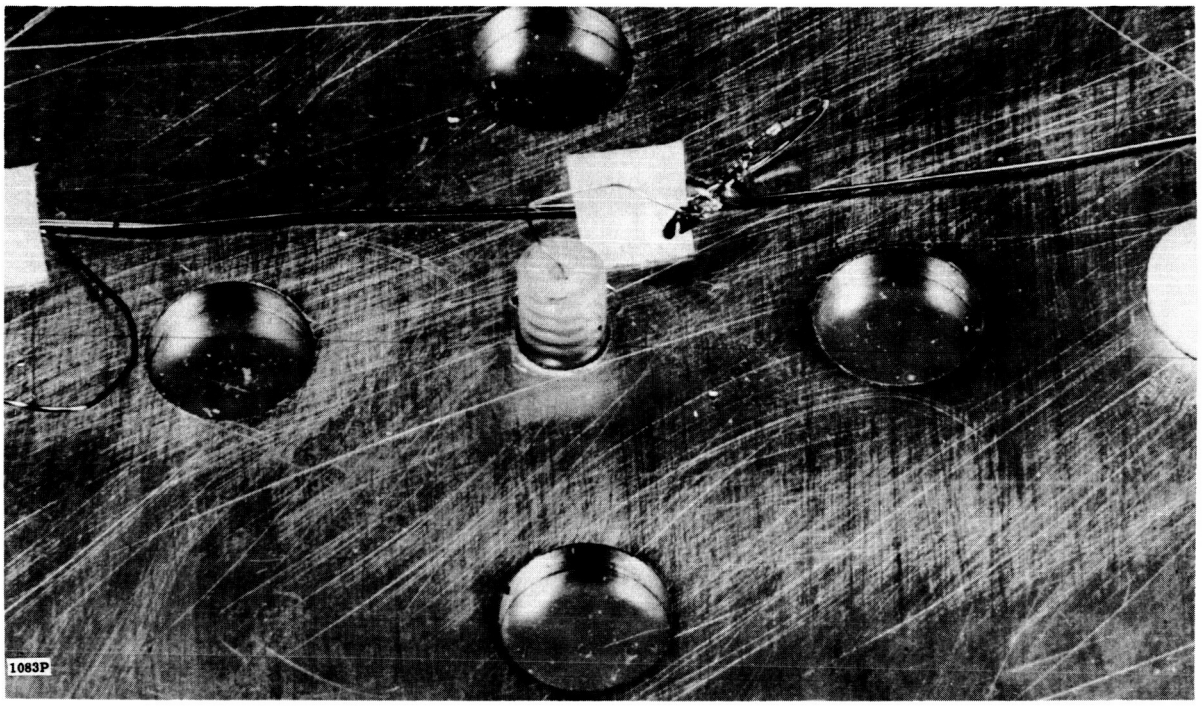

Figure 28. Nylon Screw which Supports Detector as Viewed from Back Side of Model

The center of the nylon plug is drilled out to accommodate the conductor from the bottom of the detector; the conductor leaving the top surface of the detector is a small strip of conducting paint running from the detector to the skin of the model. It should be noted that a resistance approaching 2 ohms was measured between the skin and the model. This was discussed with the personnel at Langley and arrangements were made to have a better connection made before tests. The position of the detectors can be seen in Figure 29. They are the black spots on the surface of the model. One detector is on the underside of the model and is not visible in the photograph. A front view of the model is shown in Figure 30. Figures 31 and 32 are closeups of Figures 29 and 30, respectively.

After these detectors were mounted in the model, the top surface of each element was electrically connected to the outer skin (as mentioned earlier) which serves as ground. The back face of each element was connected to individual pins of a female Winchester plug (see Figure 33) by means of No. 33 copper wire. One pin serves as ground and electrically connected to the metal housing. The female portion of the Winchester plug was mounted inside the model. The male portion was equipped with

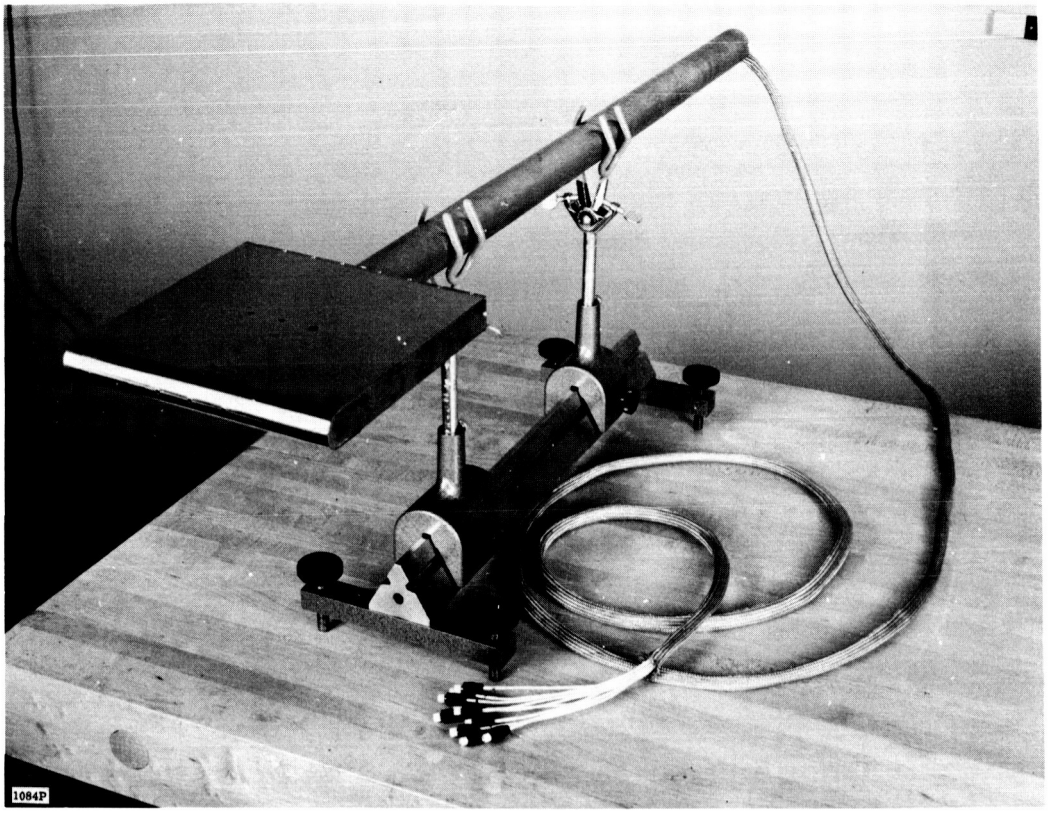

Figure 29. Completed Model with Detectors Installed. The Detectors Are the Black Spots on the Surface of the Model.

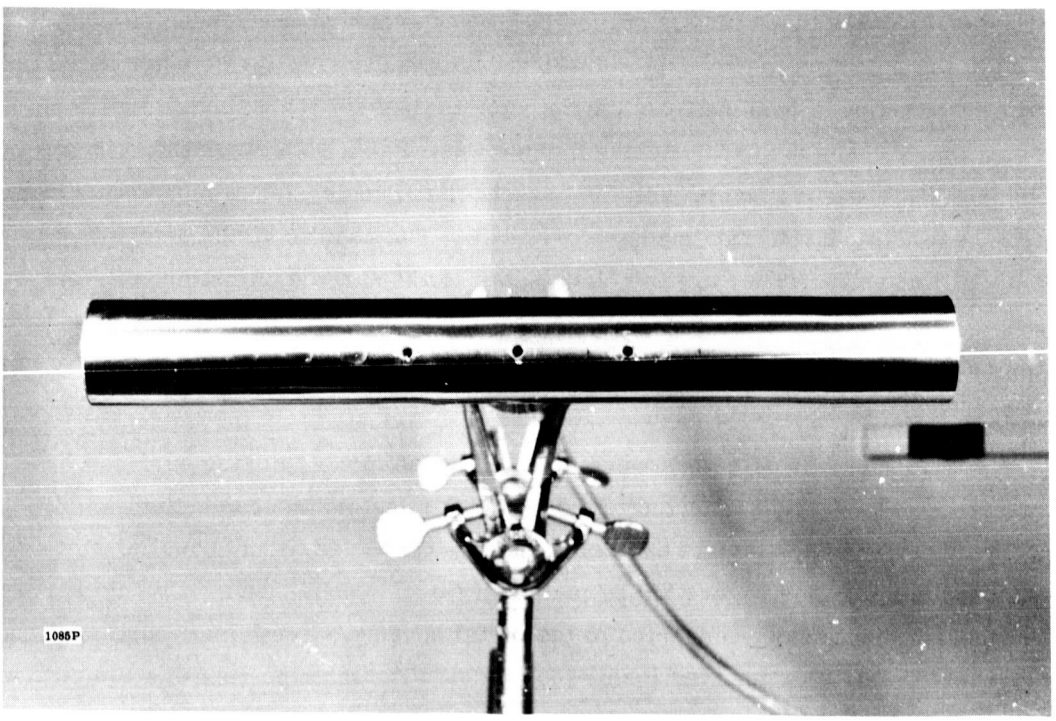

Figure 30. Front View of Completed Model

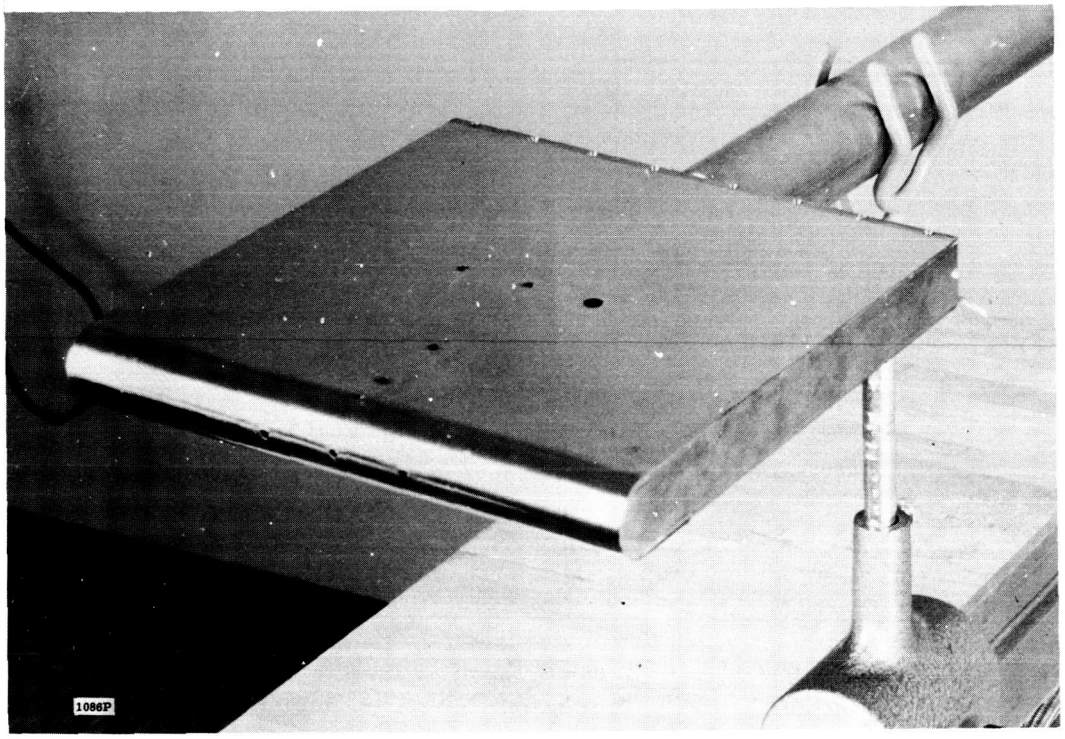

Figure 31. Closeup View of Completed Model

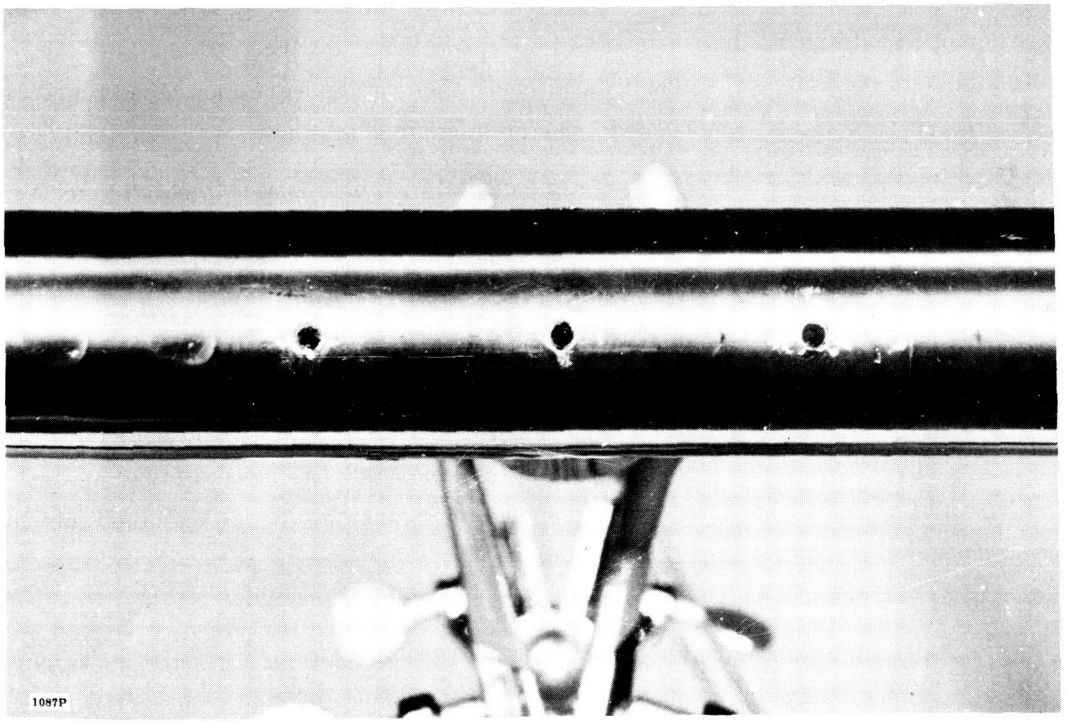

Figure 32. Closeup View of the Three Detectors on the Leading Edge of the Model

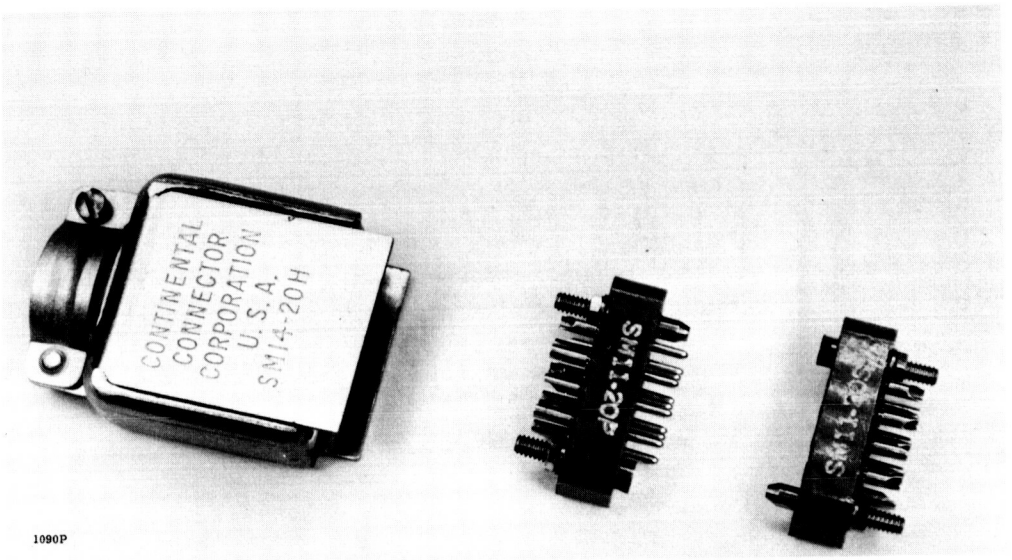

Figure 33. Winchester Plugs and Cover as Used to Connect Coaxial Leads from the Sting to Detector Leads in the Model

RF-198 coaxial cable running from each pin except the ground pin which was used as a common terminal for all shield leads. The coaxial leads were made long enough to provide 10 feet of cable after leaving the sting (i.e., the mounting tube). Each cable was equipped with an FXR connector No. 5116-037475 at its free end and labelled in accordance with the detector element monitored. The cables were then laced together and wrapped with a good conductor to provide further shielding.

The surface of the detectors were coated with black paint to obtain greater absorption of radiant energy. Aquadag was previously used for this coating, but it was observed to crack and peel when irradiated with high energy sources.

4.7.4 Calibration of Detectors

A General Electric 1200/1CL/HT heat lamp was used with an elliptical reflector similar to that shown in Figure 34 to obtain radiant energies intense enough to duplicate tunnel conditions. The total output power of this lamp was plotted against applied voltage. The resulting curve is shown in Figure 35. It was assumed that the power received from this lamp at any point in space is proportional to the total output power after the absorption region of the quartz is passed.

A detector was placed at the focal point of the elliptical reflector containing the heat lamp with a spring-loaded shutter placed between the detector and the source.

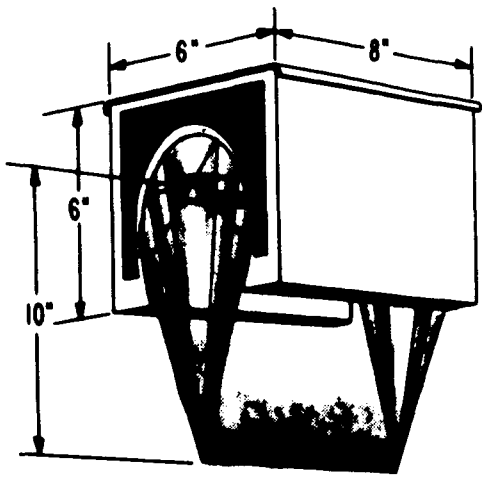

Figure 34. Stainless Steel Elliptical Reflector to Focus Radiation from 1200 Watt Infrared Heat Lamp to Obtain Energy Densities Large Enough to Calibrate Detectors Used in Hot Shot Tunnel at Langley Research Center

A single pulse was allowed to hit the detector and the magnitude of the peak voltage response was recorded. This measurement was taken as a function of total output power from the heat lamp and the results are shown in Figure 36a. The line is extrapolated on the lower end and does not go through the origin. This is due to the relatively high absorption at the long wavelengths in the quartz and does not imply that a signal would be given for zero energy. The true response in this absorptive region is shown by the dotted line at the lower end of the curve.

The detector response as a function of incident power for low powers could be measured quantitatively using a black body source. The results of these measurements are given in Figure 36b and these results are transferred to Figure 36a. The scale of Figure 36b was related to that of Figure 36a by requiring the extrapolated line from the black body data to pass through the point relating to highest power for the GE heat lamp. It is seen that the correlation between these two sets of data is quite good and illustrates the linearity between signal and incident powers into the region of 100 watts per cm^2.

The model was delivered to Langley Research Center on April 5, 1965 and all detectors were successfully checked after transporting. Each detector possessed a rise time of approximately 2 - 3 milliseconds.

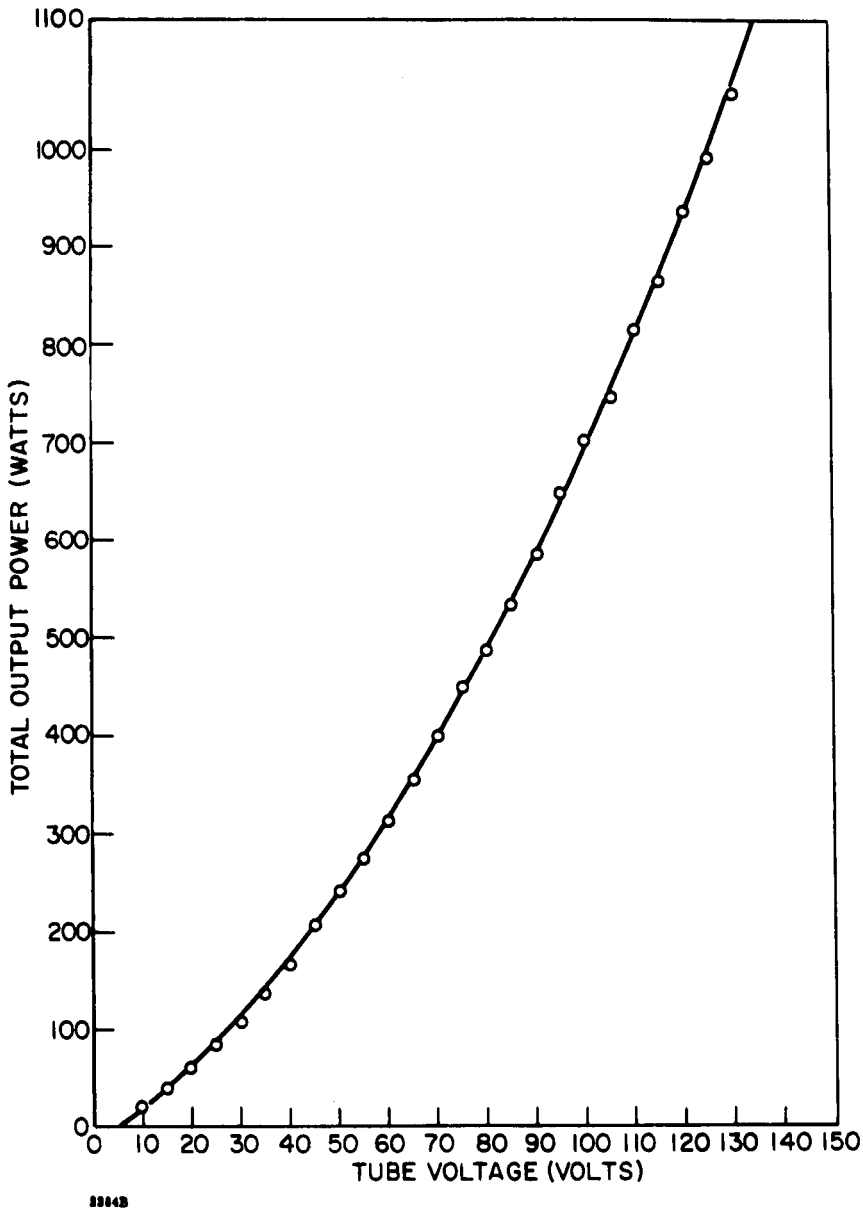

Figure 35. Total Output Power of 1200/1CL/HT Heat Lamp as a Function of Applied Voltage

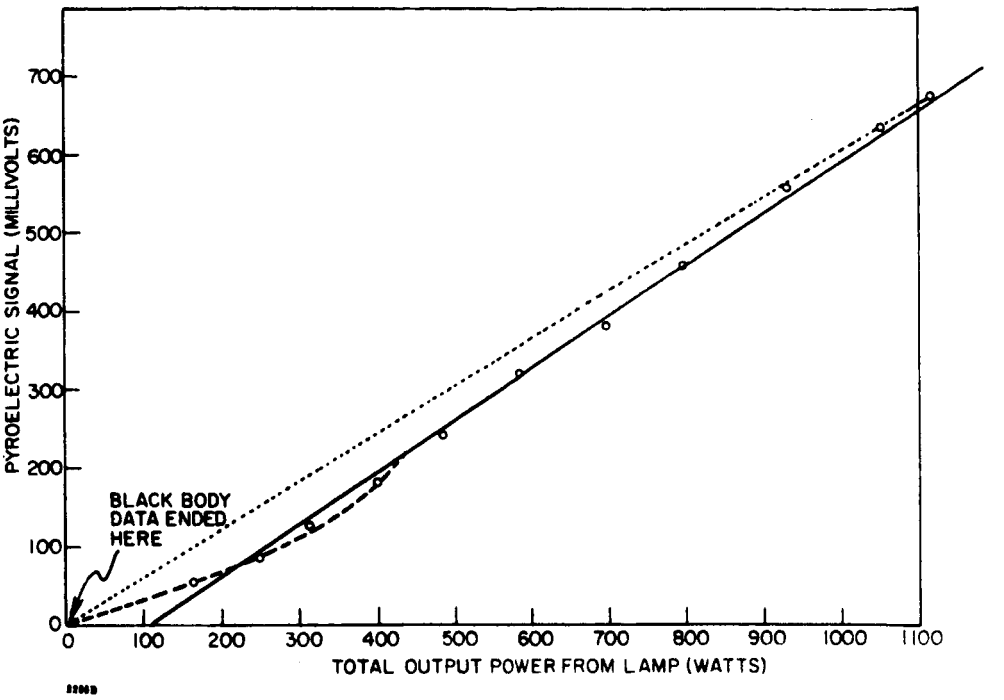

Figure 36a. Detector Output as a Function of the Total Output Power (See Figure 35) of the Heat Lamp Used for Calibration

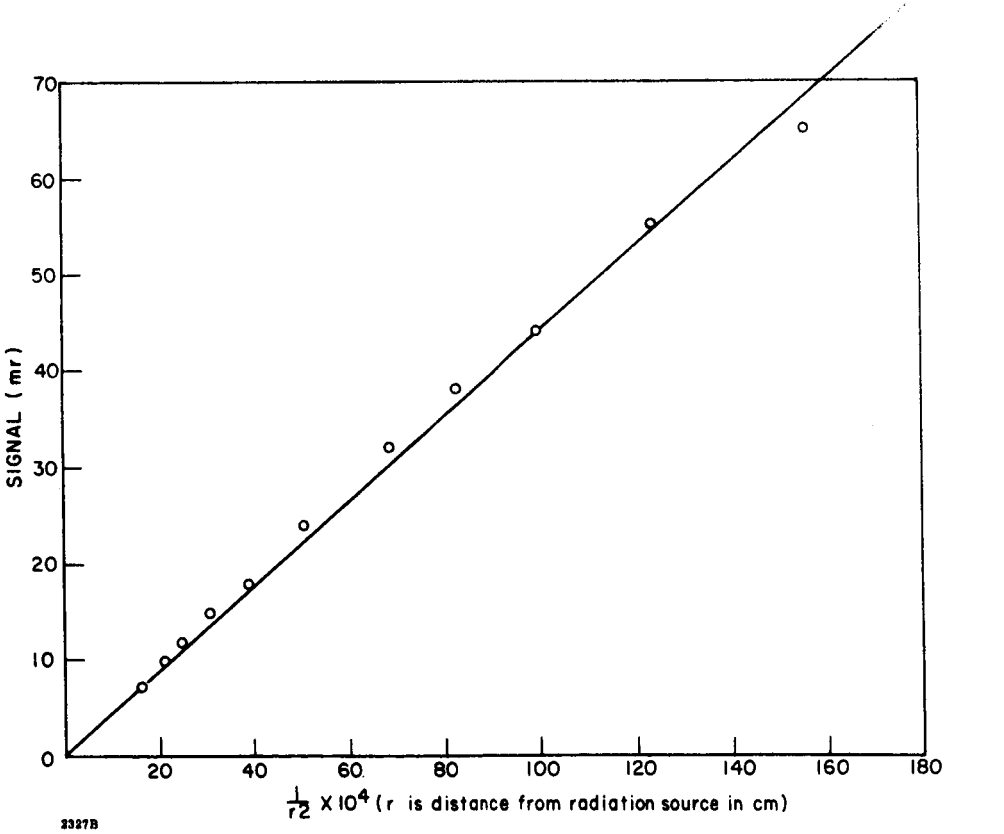

Figure 36b. Detector Response as a Function of the Inverse Square of the Distance from the Black Body Radiation Source

4.7.5 Testing of Ceramic Detectors

The shock mount tube with all detectors installed was delivered to Langley Research Center to await testing. On May 10, 1965, Mr. Hickman arrived at Langley to attend the tests scheduled in the hot shot tunnel the following day.

Inquiry regarding tunnel facilities, however, revealed that the data system at the tunnel did not have proper characteristics. This data system was a "600/DATA ACQUISITION LABORATORIES" system built by Systems Engineering Laboratories in Fort Lauderdale, Florida. The input to this system had a 1 microfarad capacitor in shunt with the source where a 1 megohm resistive input impedance had been specified.

The test was made the following day but gave no useful information. On May 12, a Sanborn recorder was found which had the right input impedance but had a dc to 100 cycle response where a dc to 20 kilocycle response had been specified. Two channels were run on this recorder, two on a Tektronix 555 dual trace oscilloscope and two more on two 545 Tektronix oscilloscopes. The two 545 scopes triggered prematurely and the 555 showed excessive noise.

The only useful information came from Detector "J" which was positioned on the underside of the model just behind the leading edge. Figure 37 shows an enlargement of the response of this detector. The peak of this curve shows a maximum power density of 5.3 watts/cm^2, which corresponded to the data given by the Cromel-Alumel thermocouples mounted in the model, and the trailing edge of the peak shows the start of subsonic flow. The figure is enlarged considerably and each small division corresponds to one millimeter. The responsivity of this detector was given in Table III which is given in Section 4.7.4 on calibration.

Another test date was scheduled so that the detectors would be tested under more favorable conditions, that is, with proper amplifiers. August 24 was the date set for the start of these tests. The detectors were recalibrated with a black body radiation source just prior to going into the tunnel to correct for any changes in their response since they were first calibrated several months previously. The response of these detectors after this second calibration is given in Table IV.

Inquiry regarding amplifiers revealed that Sanborn recorders would be used for the data from the detectors. Two Sanborn recorders, Model 320, with an input impedance of 0.5 megohms were used to record the responses of detectors H, J, K, and L. The remaining detectors were connected through six Sanborn Model 150 - 1000 Preamplifiers to two Sanborn Model 154 - 100B Recorders with four channels

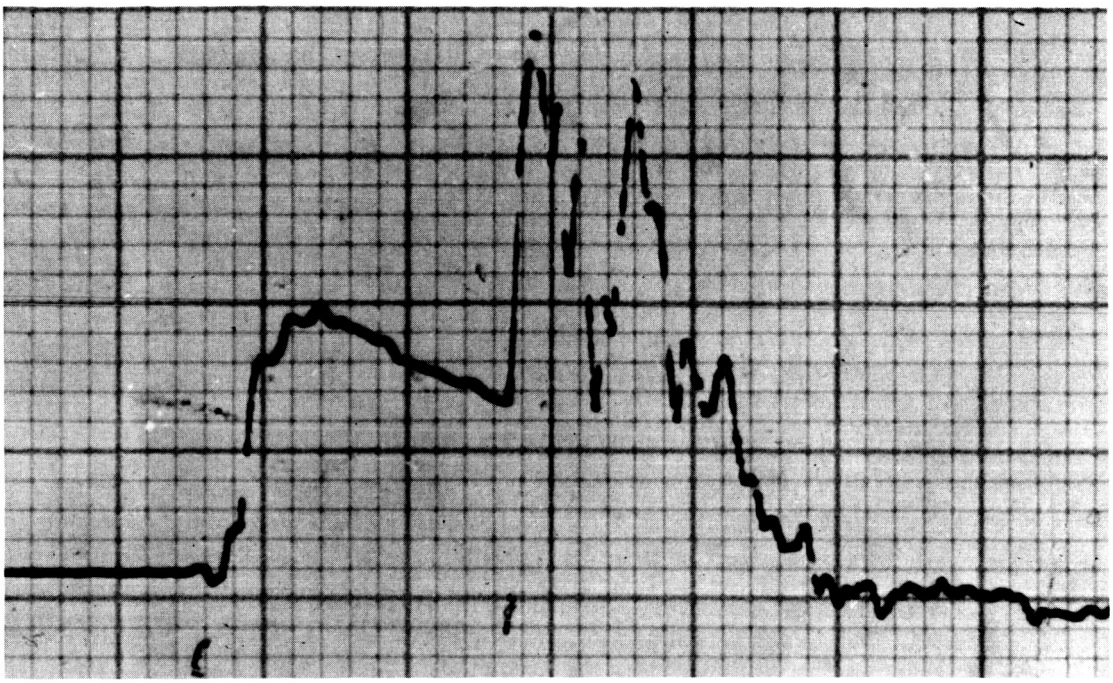

1348P

Figure 37. Data from Detector J. Horizontal Scale Is Time Scale Representing 10 Milliseconds Per Millimeter (Small Division). Vertical Scale Is Detector Response Representing 5 Millivolts Per Millimeter.

TABLE IV

Detector	Area (cm^2)	Responsivity in March 1965 at Calibration (v/w)	Responsivity on Testing Date (v/w)	Detector Output on Testing Date $mv/(w/cm^2)$
A	2.0×10^{-1}	0.131	0.186	38.0
B	5.1×10^{-2}	0.101	0.156	7.8
C	5.1×10^{-2}	0.118	0.169	8.5
D	5.1×10^{-2}	0.101	0.163	8.2
E	5.1×10^{-2}	0.101	0.149	7.5
F	5.1×10^{-2}	0.108	0.136	6.8
H	5.1×10^{-2}	0.145	0.095	4.8
J	5.1×10^{-2}	0.162	0.163	8.2
K	5.1×10^{-2}	0.148	0.116	5.8
L	5.1×10^{-2}	0.155	0.149	7.5

each. The input impedance of these systems was 5 megohms. The frequency response* of the Sanborn Model 154-100B is shown in Figures 38a and 38b. The frequency response on the Model 320 was not available.

Table V is a correction to the detector output taken from Table II as a result of the input impedances of their respective amplifiers.

TABLE V

Detector	Detector Output mv/(w/cm^2)
A	190.0
B	39.0
C	42.5
D	41.0
E	37.5
F	34.0
H	2.4
J	4.1
K	2.9
L	3.8, 7.5**

Figure 39 shows the position of each of these detectors on the model. The number by each of the letters in the figure is the average value of the maximum power densities during each run in watts/cm^2. The maximum power densities are listed individually in watts/cm^2 in Table VI for each detector and each run.

Thermocouples were placed at various places on the model to check the results from the detectors. As of this writing, however, the data from the thermocouples have not been received and a comparison is not yet possible. The data from the detectors will be given in the form of enlarged photographs of the original traces. These photographs show a grid in the background, the original scale of which was one millimeter per small division. A total of 5 runs were made and the photographs are given in Figures 40 through 72. The following comments should be made concerning detectors. Detector K was destroyed in the first run due to a direct hit from a piece of the mylar diaphragm. "C" did not function until the last run when the contact

*Taken from Sanborn Instruction Manual for 150 Series Recorder.

**The 7.5 mv/(w/cm^2) pertains to run 5 only. The amplifier had a 1 megohm input impedance for the amplification used on this run only.

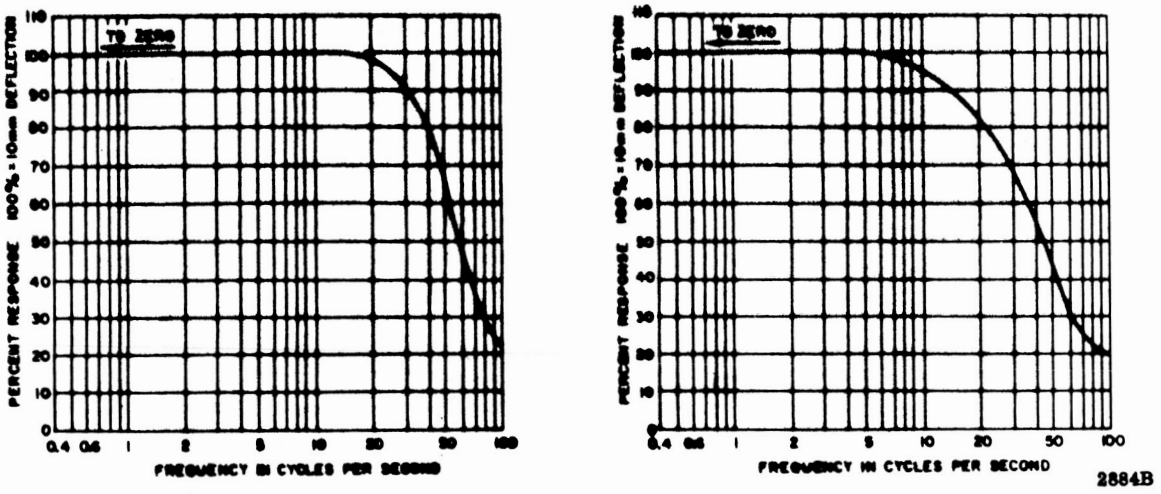

a. Characteristics at 71% of Critical Damping

b. Characteristics at Critical Damping

Figure 38. Sanborn 150 Series Recorder Galvanometer Characteristics

TABLE VI

DETECTOR NUMBER	RUN NUMBER 1	2	3	4	5
A	1.6	1.4	1.8	1.6	1.5
B	1.8	1.8	2.1	2.1	1.7
C	-	-	-	-	2.0
D	3.3	2.6	3.1	3.1	3.4
E	2.0	1.9	2.3	2.1	1.6
F	4.6	4.4	4.3	4.6	3.4
H	-	-	-	79	100
J	5.8	4.4	5.4	5.6	6.1
K	-	-	-	-	-
L	-	-	-	100	106

Maximum energy density in watts/cm^2 for each detector for each run.

between the outer electrode and the skin was reinforced with silver paint. "H" and "L" pegged the amplifiers in the first three runs. The amplification of the signal from these detectors were adjusted after each of these runs and finally the proper setting was found for the last two runs. The tape containing traces from "H" and "J" for run 5 was damaged in removing it from the recorder and consequently is not available.

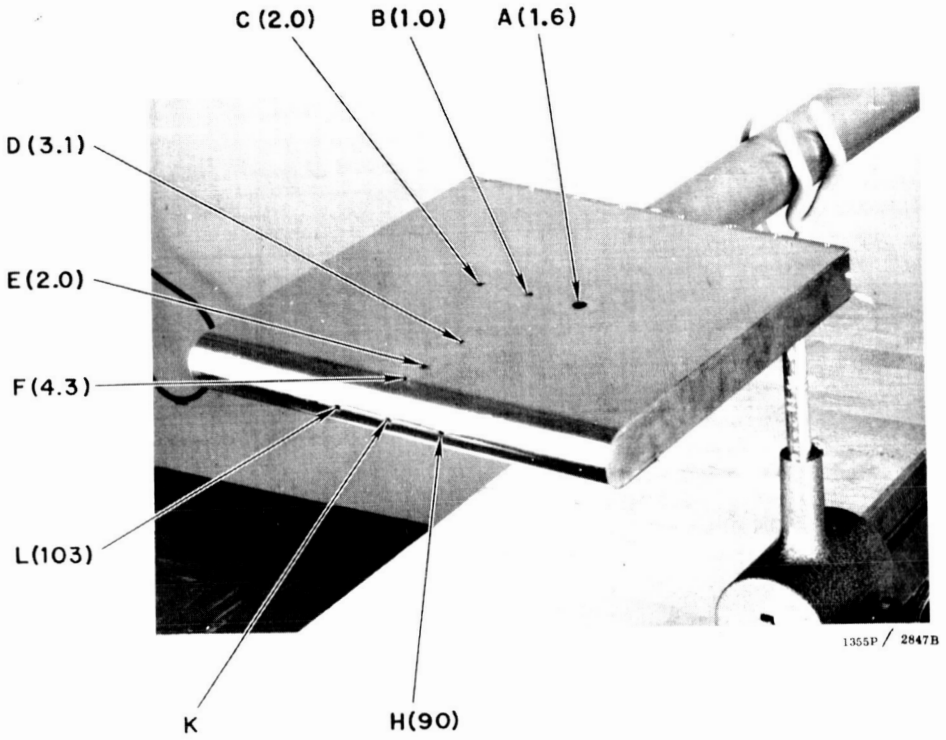

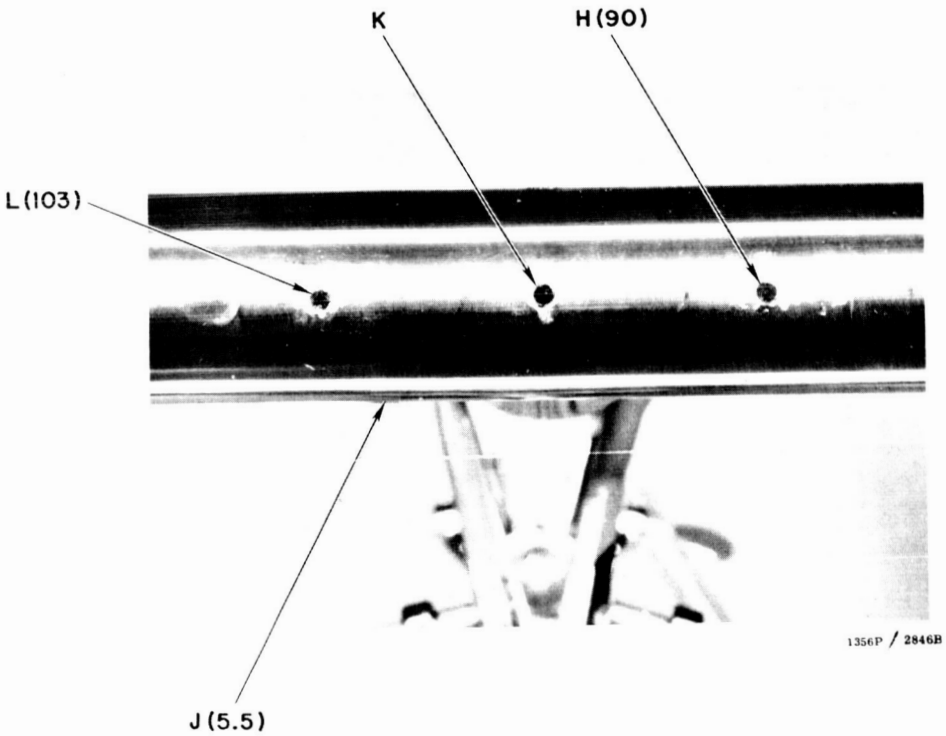

Figure 39. Closeup Views of Completed Model Showing Positions of Detectors

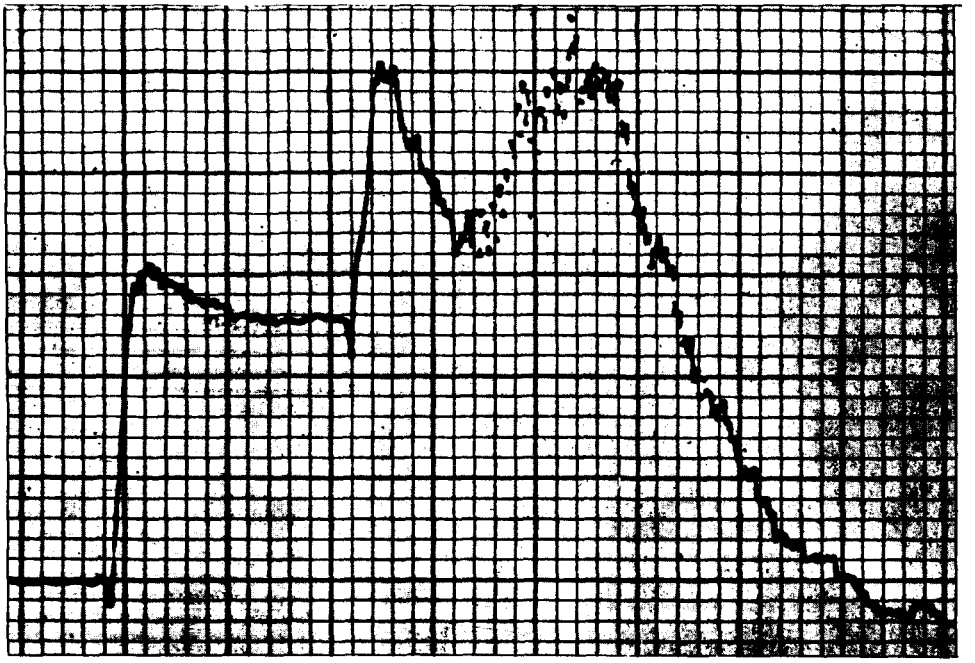

Figure No. 40. Response from Detector No. A, Run No. 1.
Horizontal Scale Represents Time Increasing from Left to Right at 100 mm/sec.
Vertical Scale Is Voltage Output Set at 20 mv/mm.

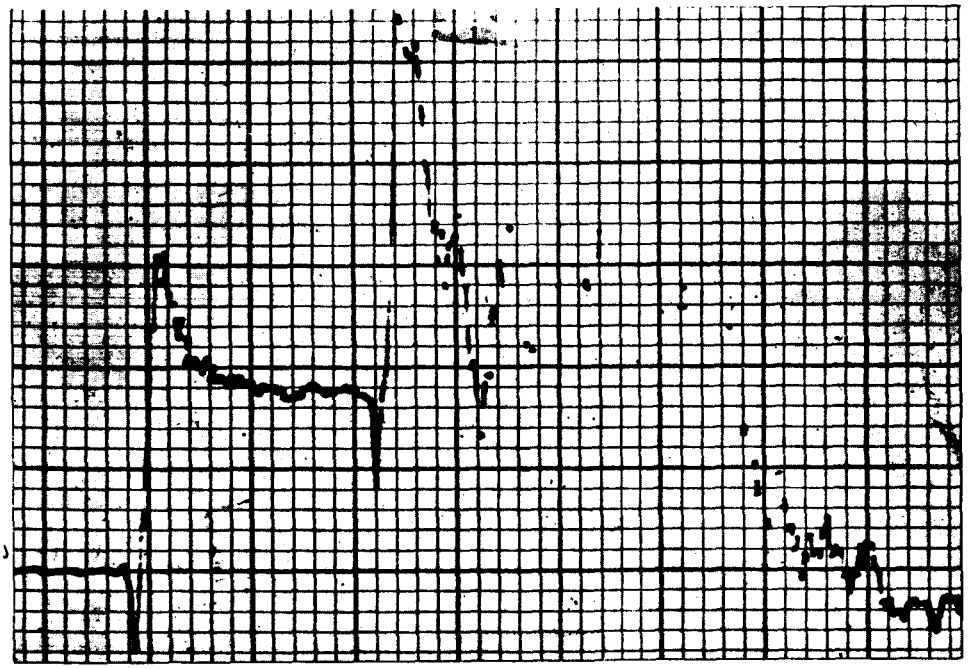

Figure No. 41. Response from Detector No. B, Run No. 1.
Horizontal Scale Represents Time Increasing from Left to Right at 100 mm/sec.
Vertical Scale Is Voltage Output Set at 5 mv/mm.

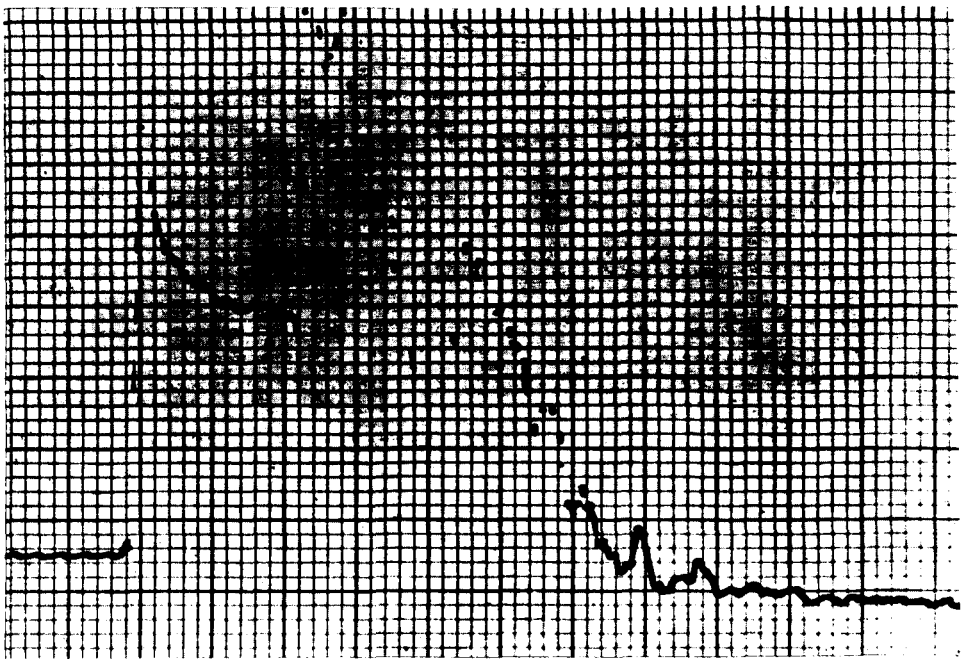

Figure No. 42. Response from Detector No. D, Run No. 1.
Horizontal Scale Represents Time Increasing from Left to Right at 100 mm/sec.
Vertical Scale Is Voltage Output Set at 5 mv/mm.

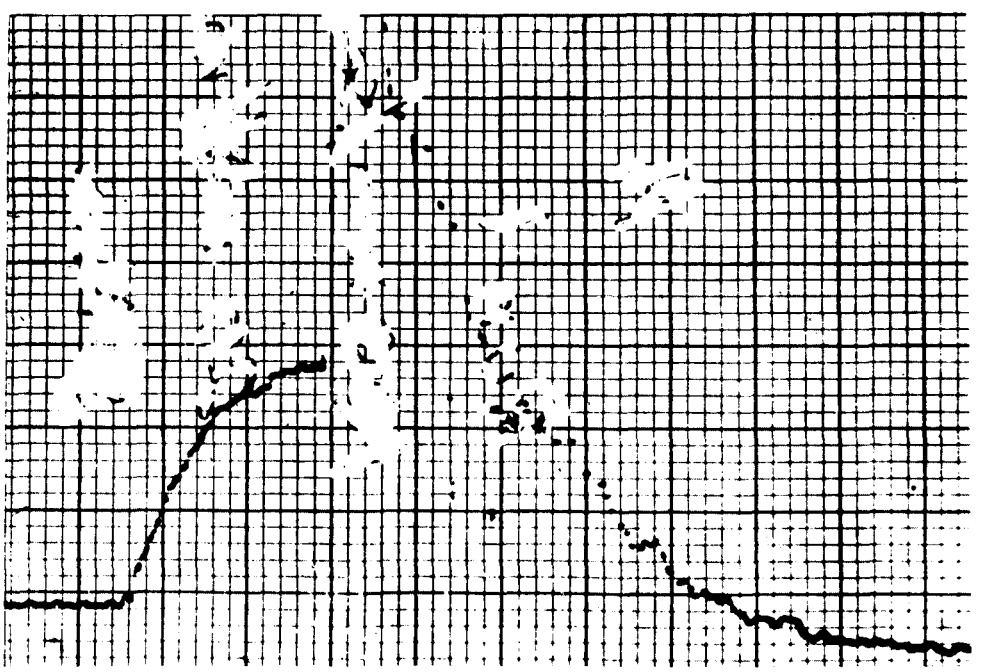

1282P

Figure 43. Response from Detector No. E, Run No. 1.
Horizontal Scale Represents Time Increasing from Left to Right at 100 mm/sec.
Vertical Scale Is Voltage Output Set at 5 mv/mm.

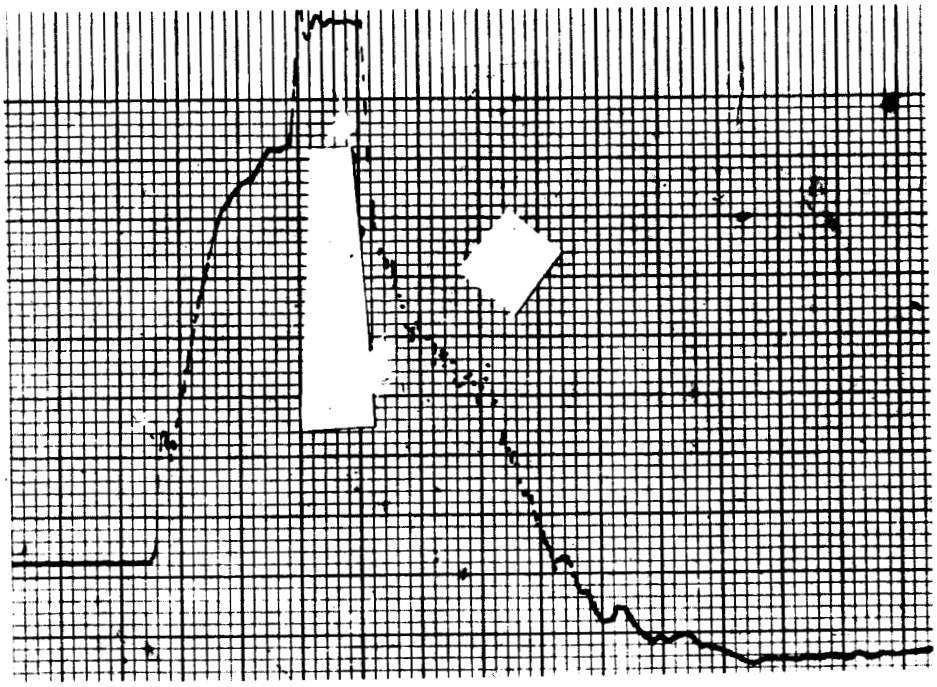

Figure No. 44. Response from Detector No. F, Run No. 1.
Horizontal Scale Represents Time Increasing from Left to Right at 100 mm/sec.
Vertical Scale Is Voltage Output Set at 5 mv/mm.

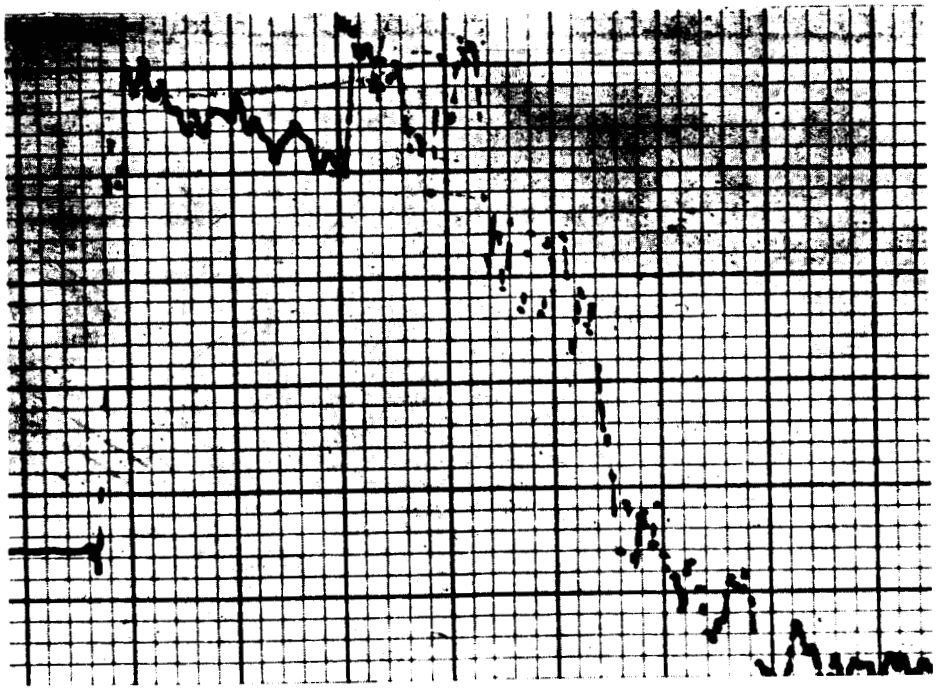

Figure No. 45. Response from Detector No. J, Run No. 1. 1294P
Horizontal Scale Represents Time Increasing from Left to Right at 100 mm/sec.
Vertical Scale Is Voltage Output Set at 1 mv/mm.

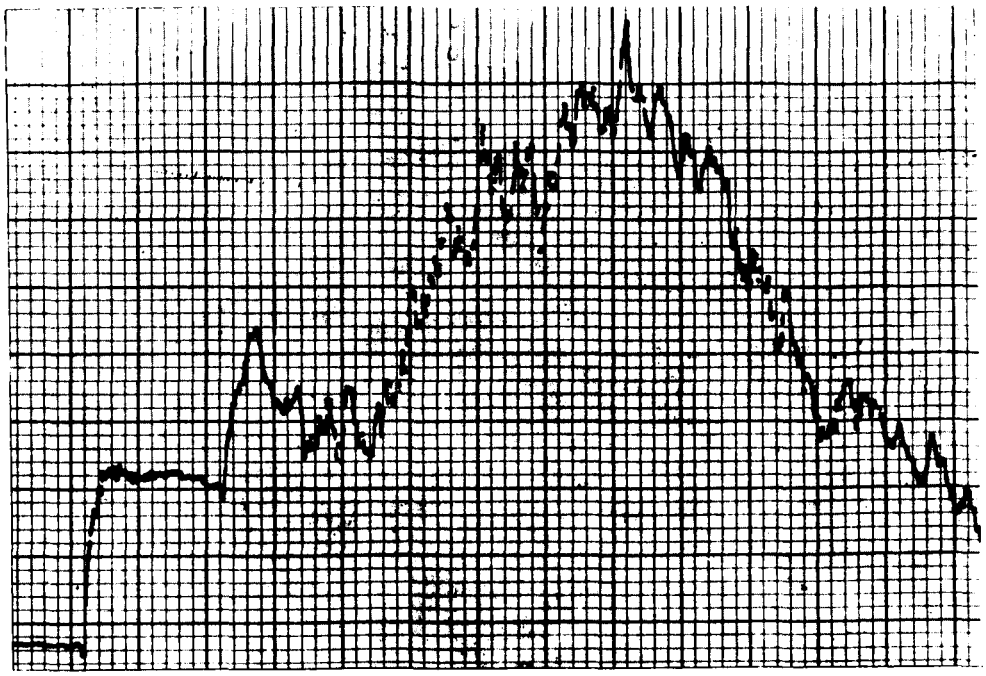

Figure No. 46. Response from Detector No. A, Run No. 2.
Horizontal Scale Represents Time Increasing from Left to Right at 100 mm/sec.
Vertical Scale Is Voltage Output Set at 20 mv/mm.

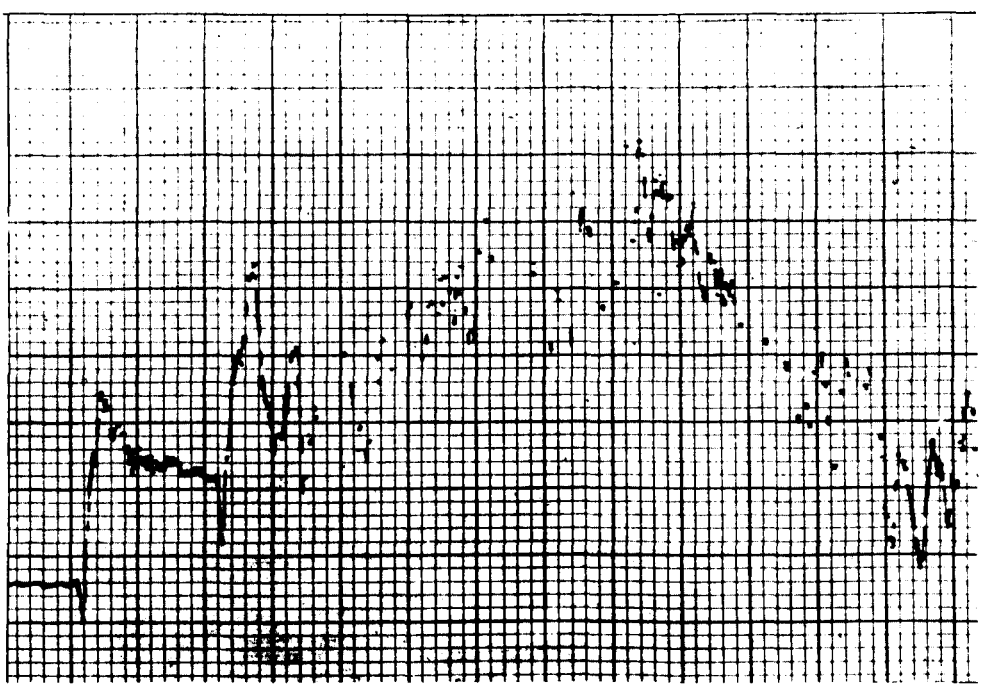

Figure No. 47. Response from Detector No. B, Run No. 2. 1297P
Horizontal Scale Represents Time Increasing from Left to Right at 100 mm/sec.
Vertical Scale Is Voltage Output Set at 5 mv/mm.

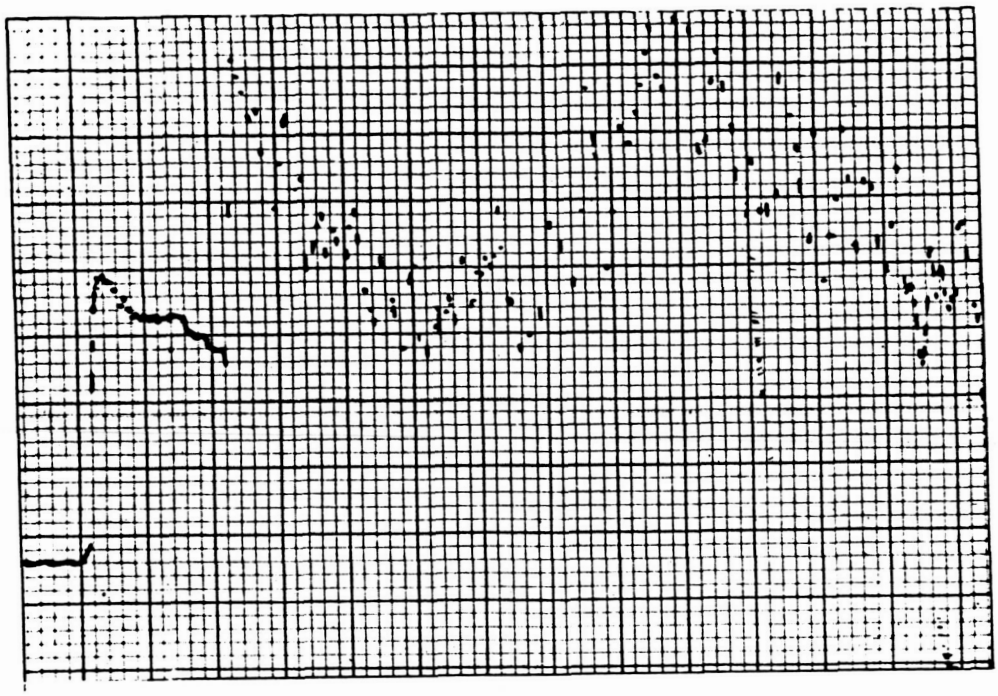

Figure No. 48. Response from Detector No. D, Run No. 2.
Horizontal Scale Represents Time Increasing from Left to Right at 100 mm/sec.
Vertical Scale Is Voltage Output Set at 5 mv/mm.

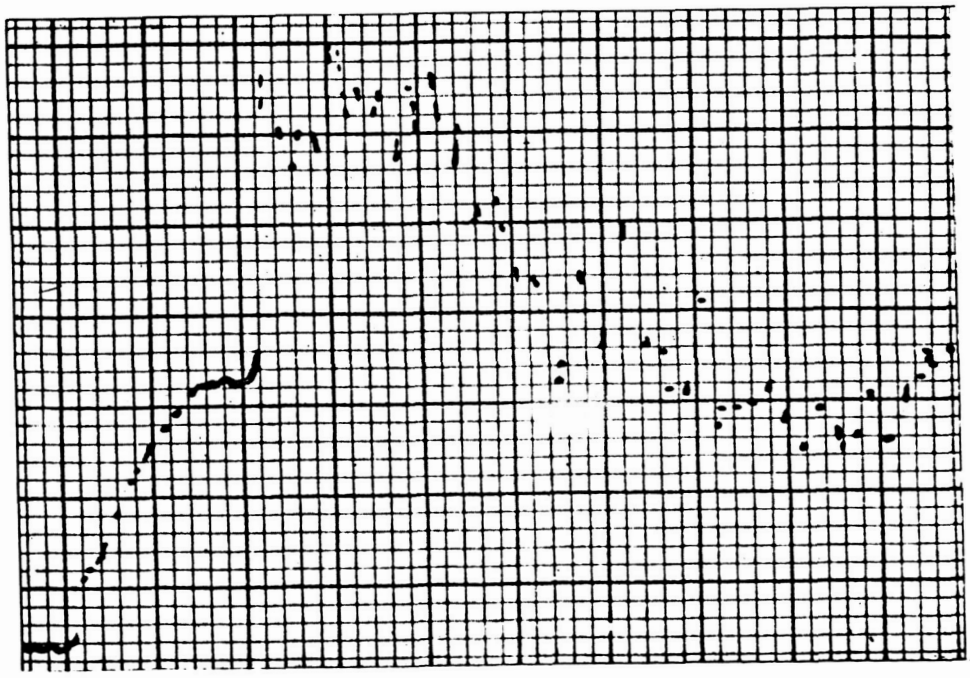

Figure No. 49. Response from Detector No. E, Run No. 2. 1294P
Horizontal Scale Represents Time Increasing from Left to Right at 100 mm/sec.
Vertical Scale Is Voltage Output Set at 5 mv/mm.

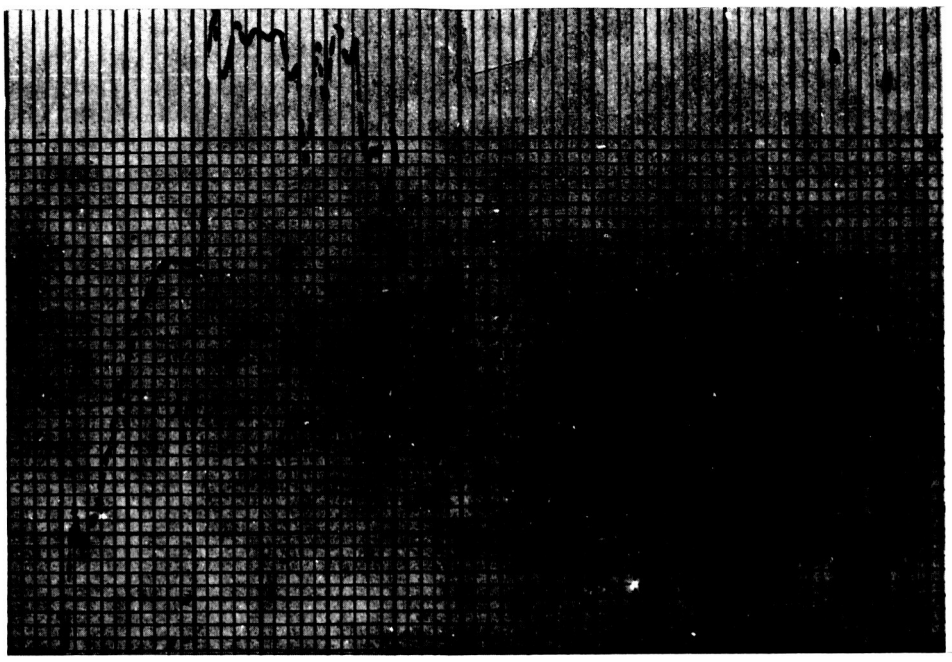

Figure No. 50. Response from Detector No. F, Run No. 2.
Horizontal Scale Represents Time Increasing from Left to Right at 100 mm/sec.
Vertical Scale Is Voltage Output Set at 5 mv/mm.

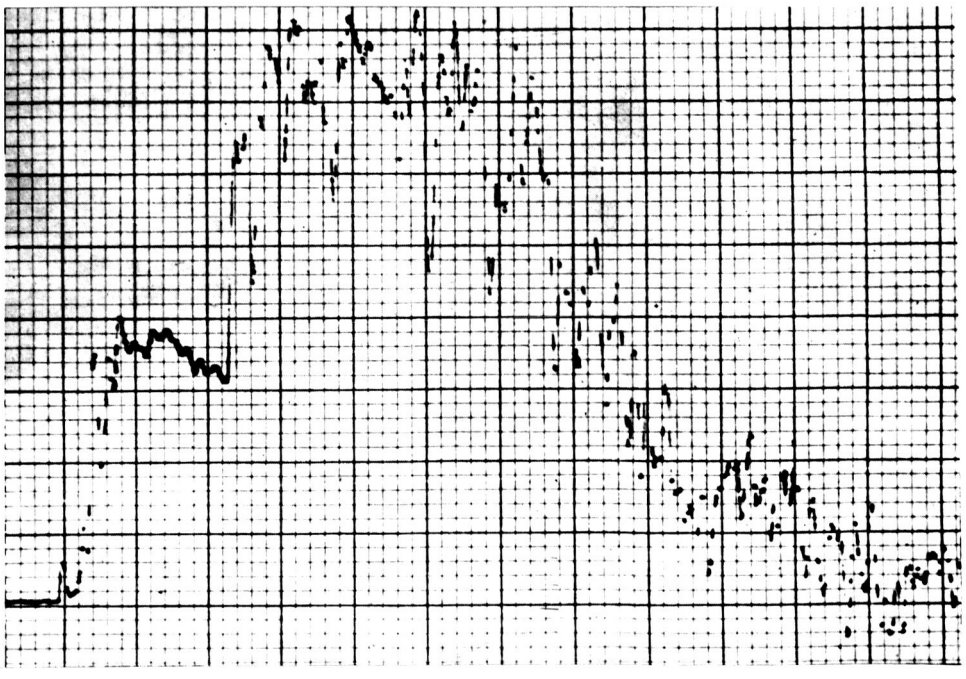

Figure No. 51. Response from Detector No. J, Run No. 2. 1361P
Horizontal Scale Represents Time Increasing from Left to Right at 100 mm/sec.
Vertical Scale Is Voltage Output Set at 1 mv/mm.

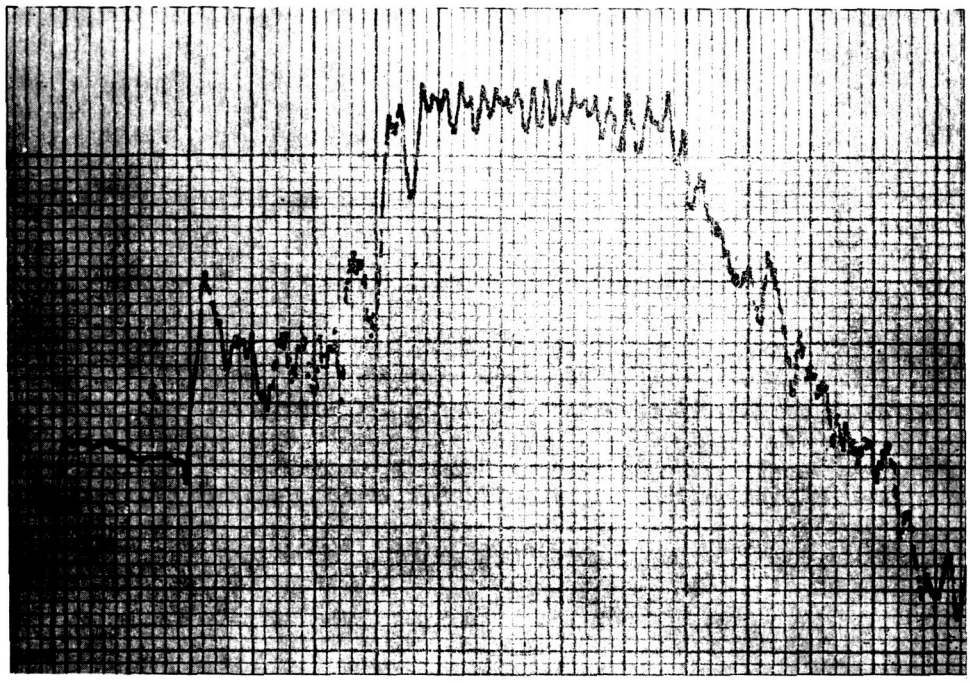

Figure No. 52. Response from Detector No. A, Run No. 3.
Horizontal Scale Represents Time Increasing from Left to Right at 100 mm/sec.
Vertical Scale Is Voltage Output Set at 20 mv/mm.

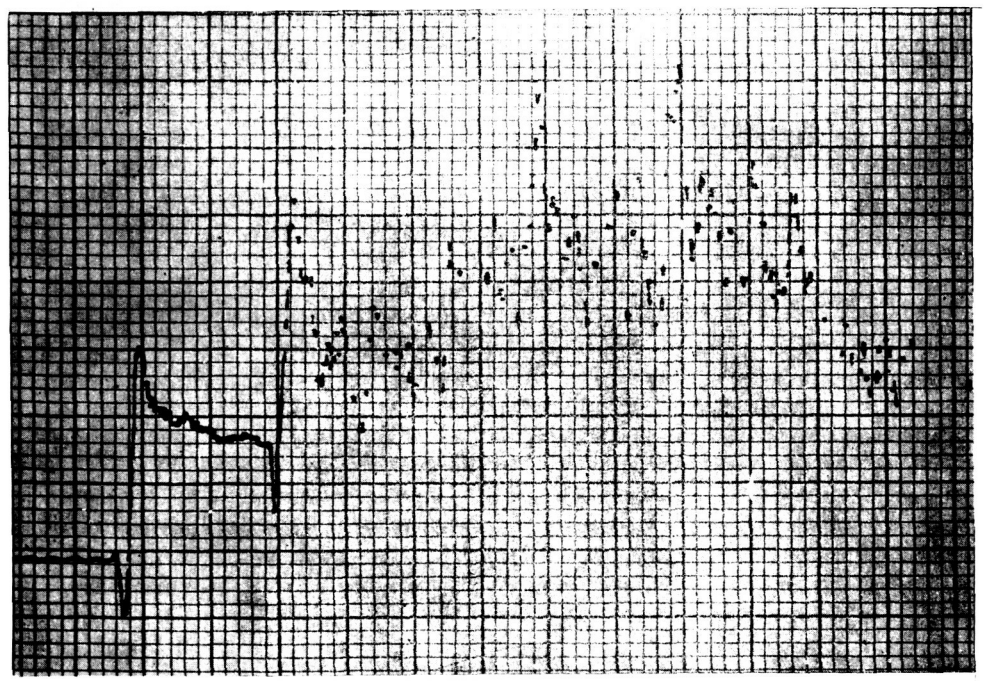

Figure No. 53. Response from Detector No. B, Run No. 3. 1307P
Horizontal Scale Represents Time Increasing from Left to Right at 100 mm/sec.
Vertical Scale Is Voltage Output Set at 5 mv/mm.

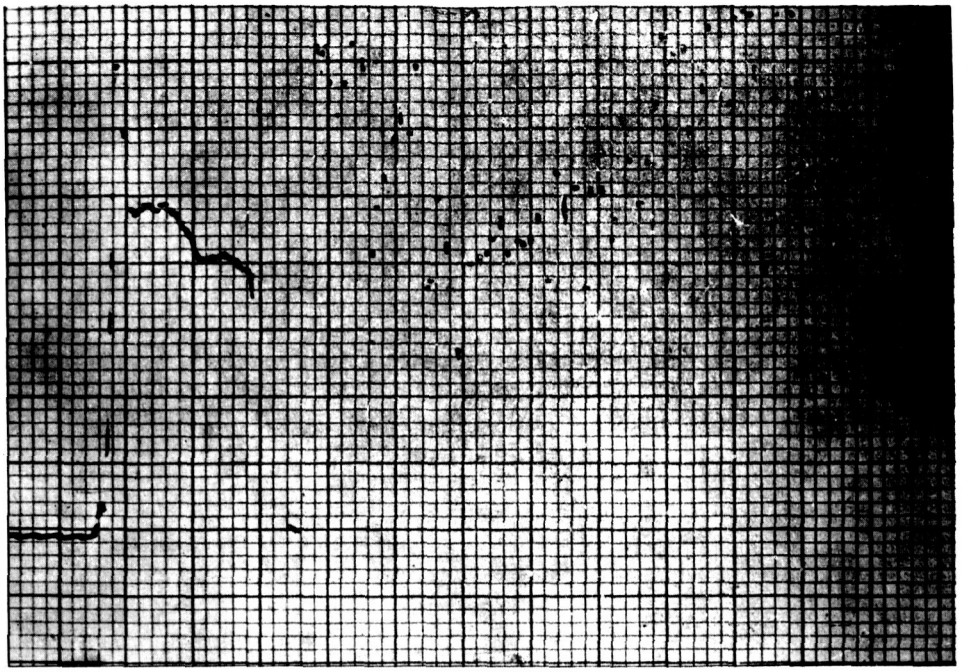

Figure No. 54. Response from Detector No. D, Run No. 3.
Horizontal Scale Represents Time Increasing from Left to Right at 100 mm/sec.
Vertical Scale Is Voltage Output Set at 5 mv/mm.

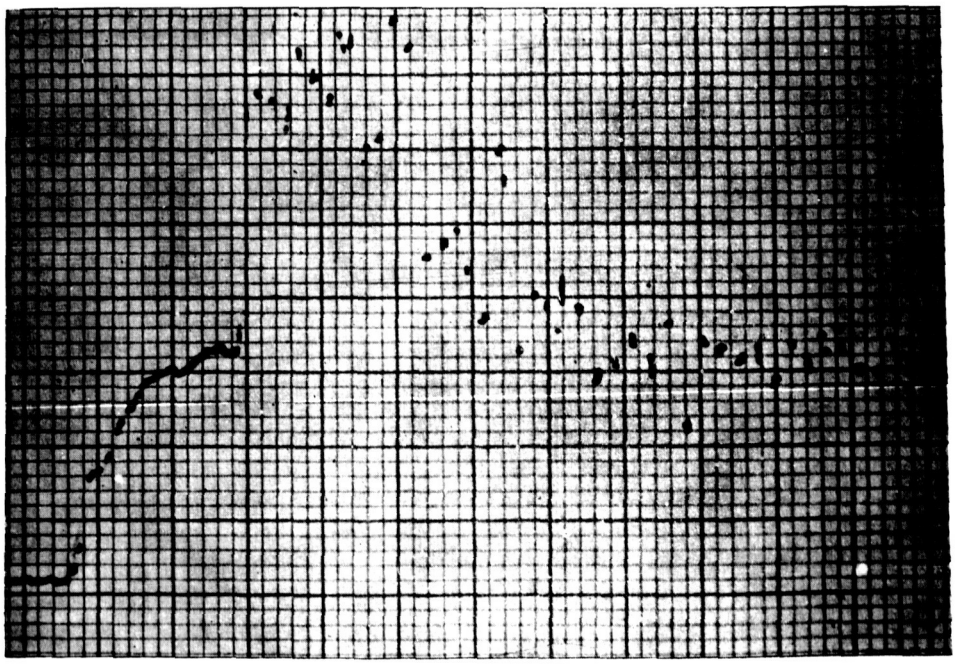

Figure No. 55. Response from Detector No. E, Run No. 3_{I293P}
Horizontal Scale Represents Time Increasing from Left to Right at 100 mm/sec.
Vertical Scale Is Voltage Output Set at 5 mv/mm.

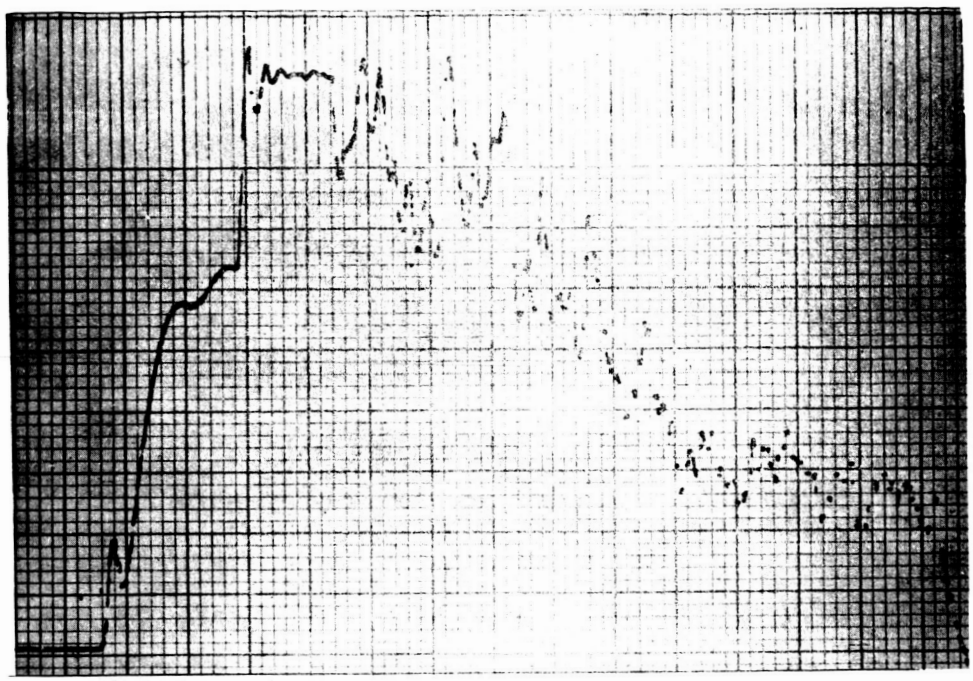

Figure No. 56. Response from Detector No. F, Run No. 3.
Horizontal Scale Represents Time Increasing from Left to Right at 100 mm/sec.
Vertical Scale Is Voltage Output Set at 5 mv/mm.

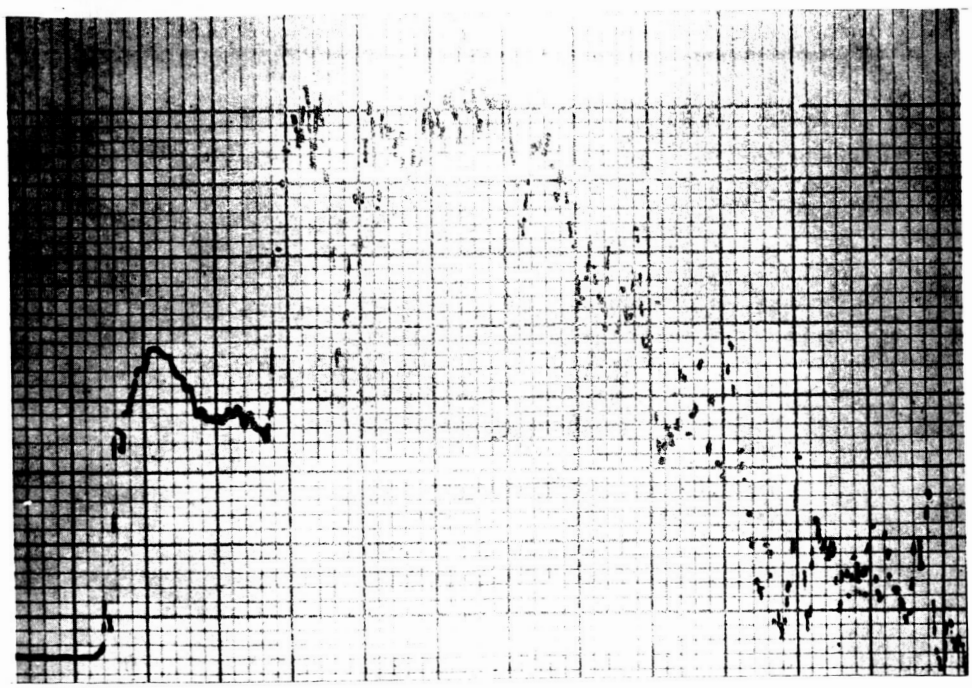

1290P

Figure No. 57. Response from Detector No. J, Run No. 3.
Horizontal Scale Represents Time Increasing from Left to Right at 100 mm/sec.
Vertical Scale Is Voltage Output at 1 mv/mm.

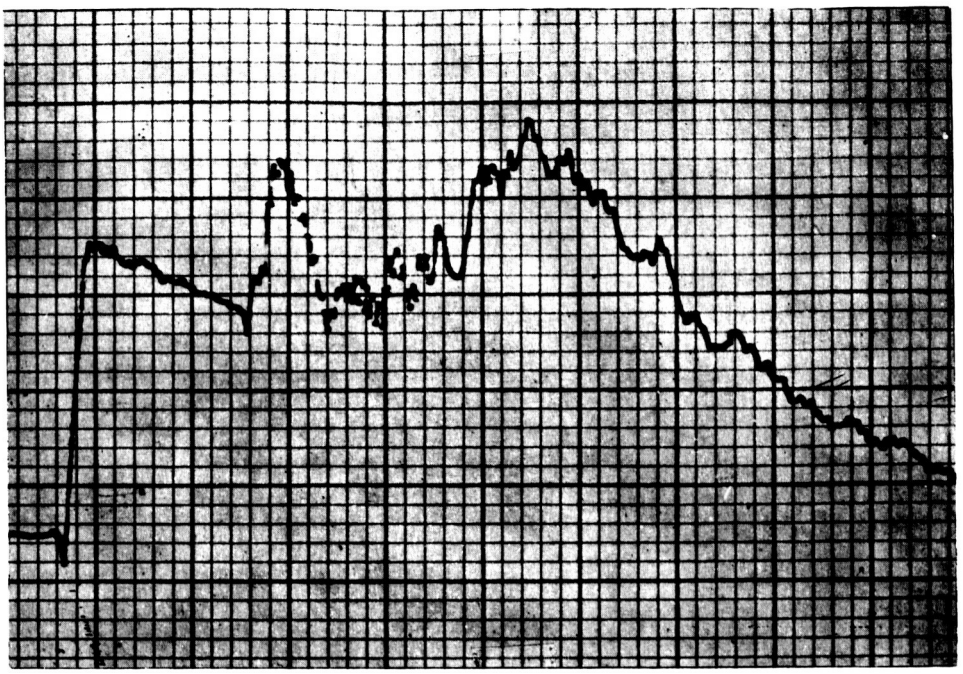

Figure No. 58. Response from Detector No. A, Run No. 4.
Horizontal Scale Represents Time Increasing from Left to Right at 100 mm/sec.
Vertical Scale Is Voltage Output Set at 20 mv/mm.

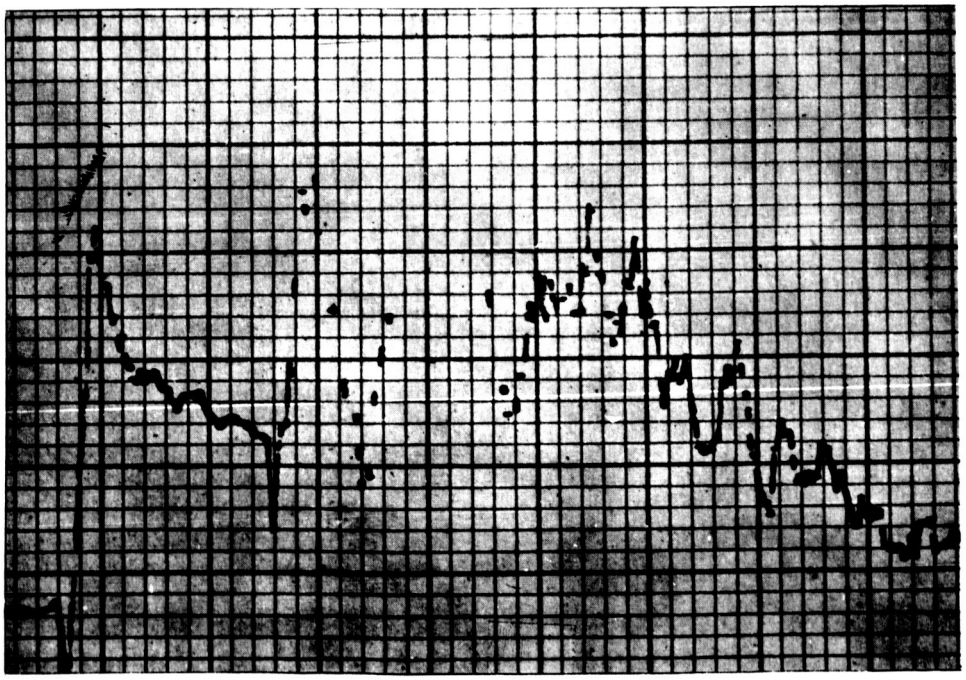

Figure No. 59. Response from Detector No. B, Run No. 4. 1291P
Horizontal Scale Represents Time Increasing from Left to Right at 100 mm/sec.
Vertical Scale Is Voltage Output Set at 5 mv/mm.

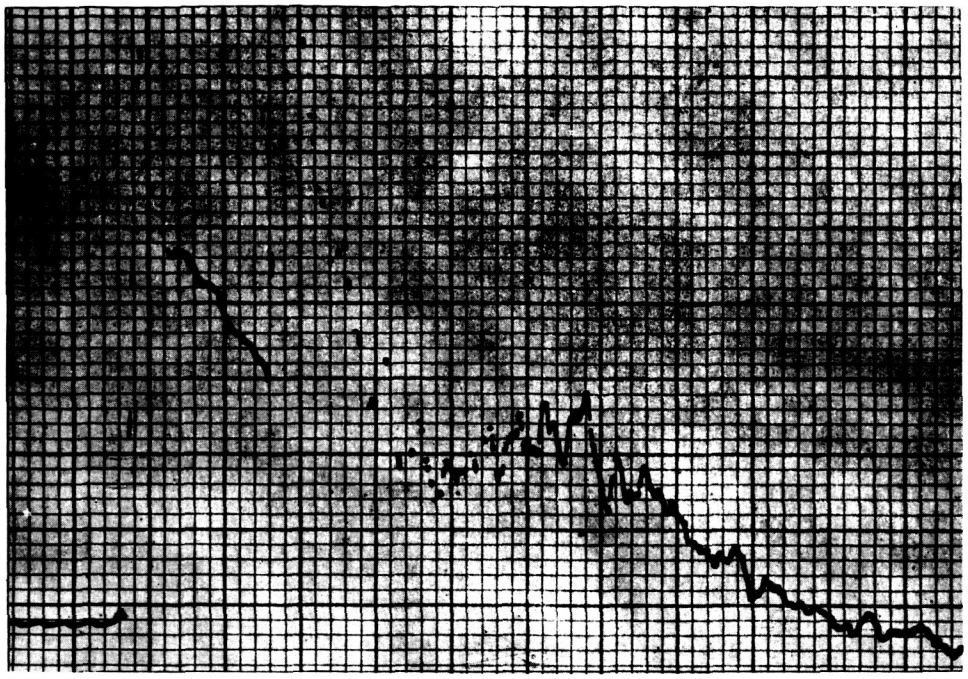

Figure No. 60. Response from Detector No. D, Run No. 4.
Horizontal Scale Represents Time Increasing from Left to Right at 100 mm/sec.
Vertical Scale Is Voltage Output Set at 5 mv/mm.

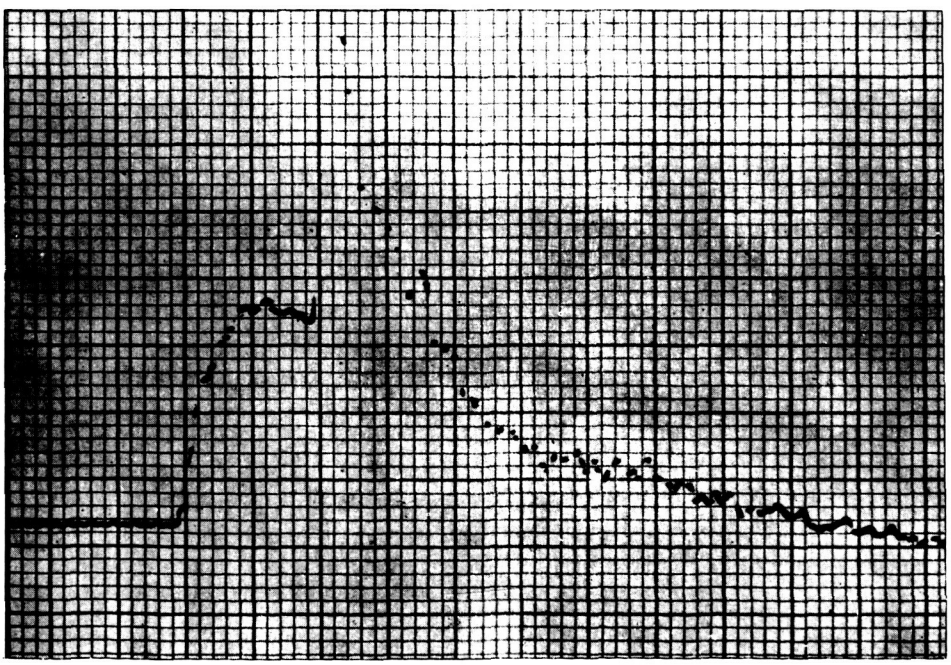

Figure No. 61. Response from Detector No. E, Run No. 4. 1304P
Horizontal Scale Represents Time Increasing from Left to Right at 100 mm/sec.
Vertical Scale Is Voltage Output Set at 5 mv/mm.

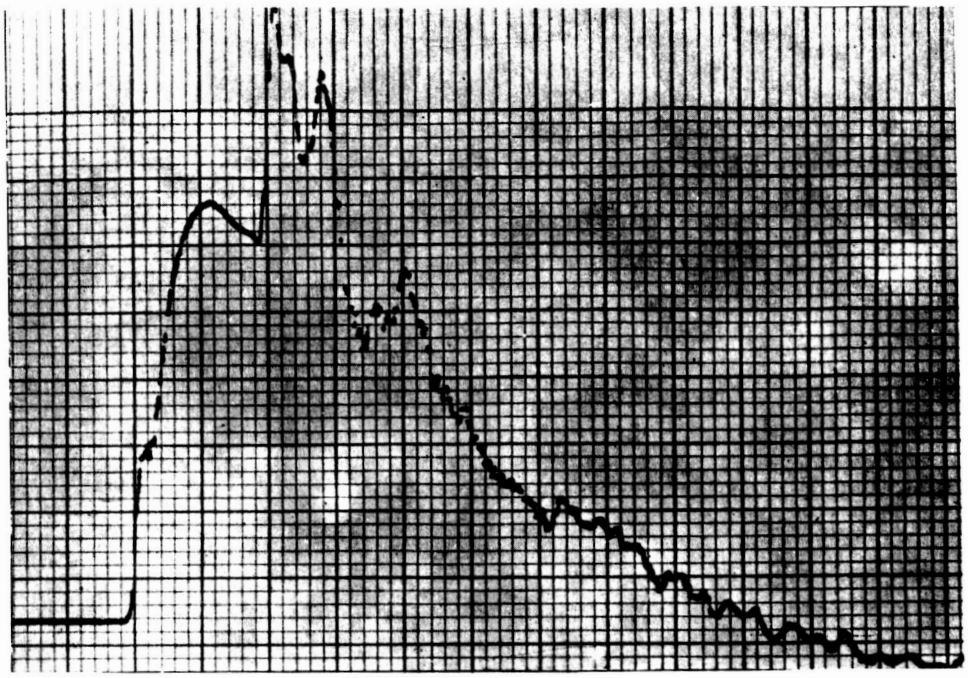

Figure No. 62. Response from Detector No. F, Run No. 4.
Horizontal Scale Represents Time Increasing from Left to Right at 100 mm/sec.
Vertical Scale Is Voltage Output Set at 5 mv/mm.

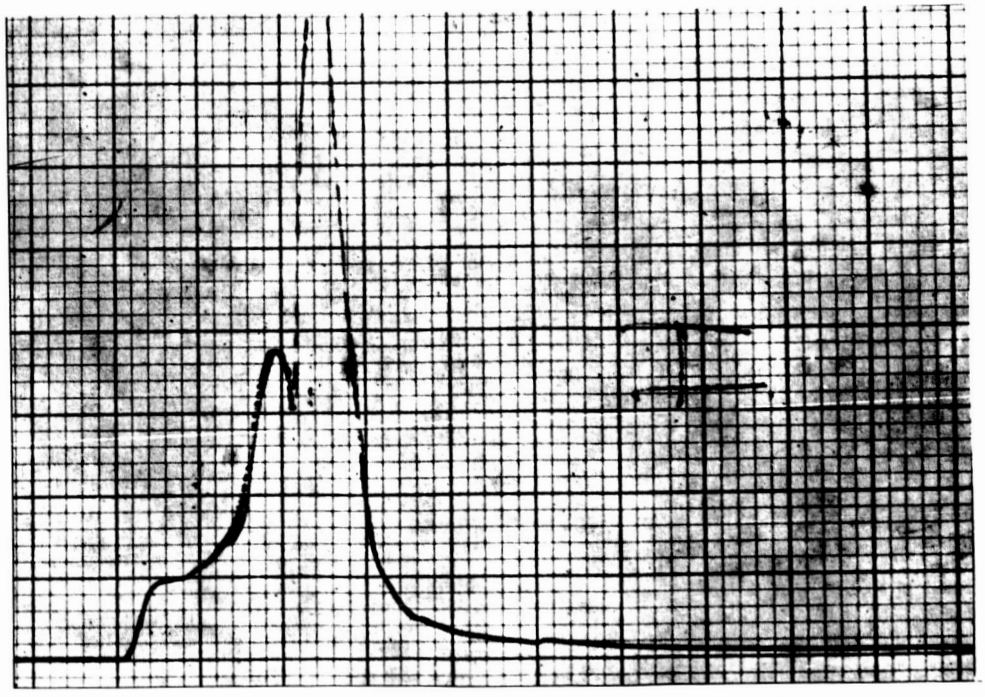

Figure No. 63. Response from Detector No. H, Run No. 4_{1305P}
Horizontal Scale Represents Time Increasing from Left to Right at 100 mm/sec.
Vertical Scale Is Voltage Output Set at 20 mv/mm.

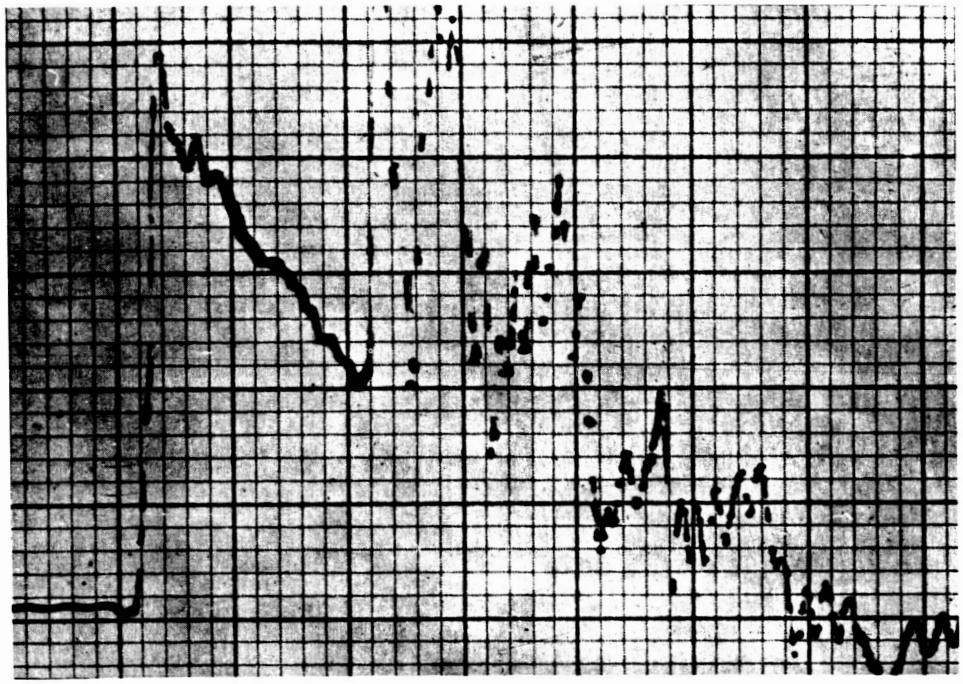

Figure No. 64. Response from Detector No. J, Run No. 4.
Horizontal Scale Represents Time Increasing from Left to Right at 100 mm/sec.
Vertical Scale Is Voltage Output Set at 1 mv/mm.

Figure No. 65. Response from Detector No. L, Run No. 4. 1303P
Horizontal Scale Represents Time Increasing from Left to Right at 100 mm/sec.
Vertical Scale Is Voltage Output Set at 20 mv/mm.

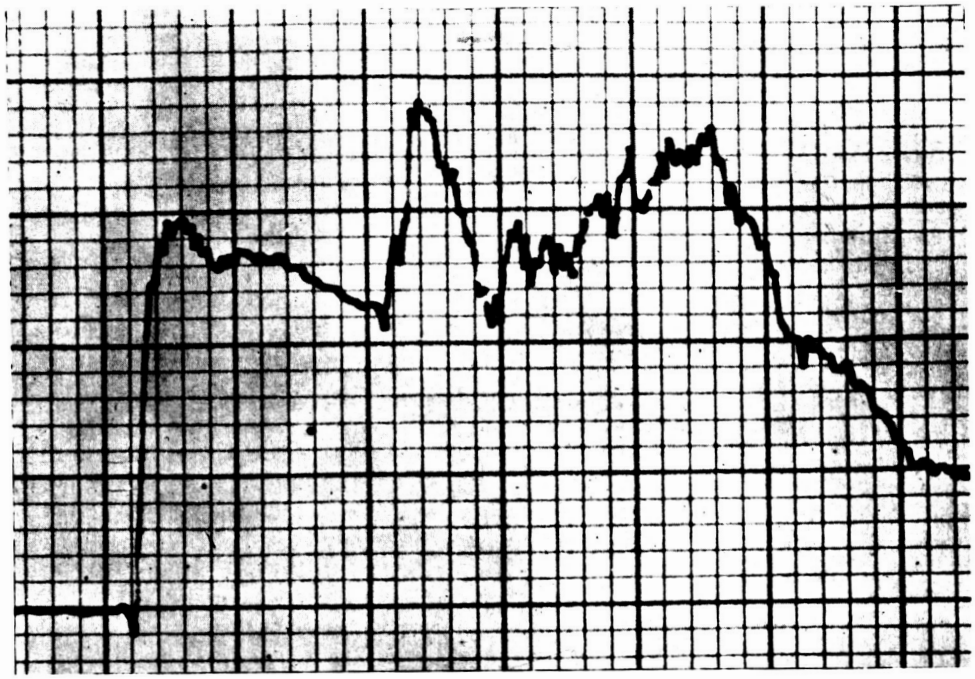

Figure No. 66. Response from Detector No. A, Run No. 5.
Horizontal Scale Represents Time Increasing from Left to Right at 100 mm/sec.
Vertical Scale Is Voltage Output Set at 20 mv/mm.

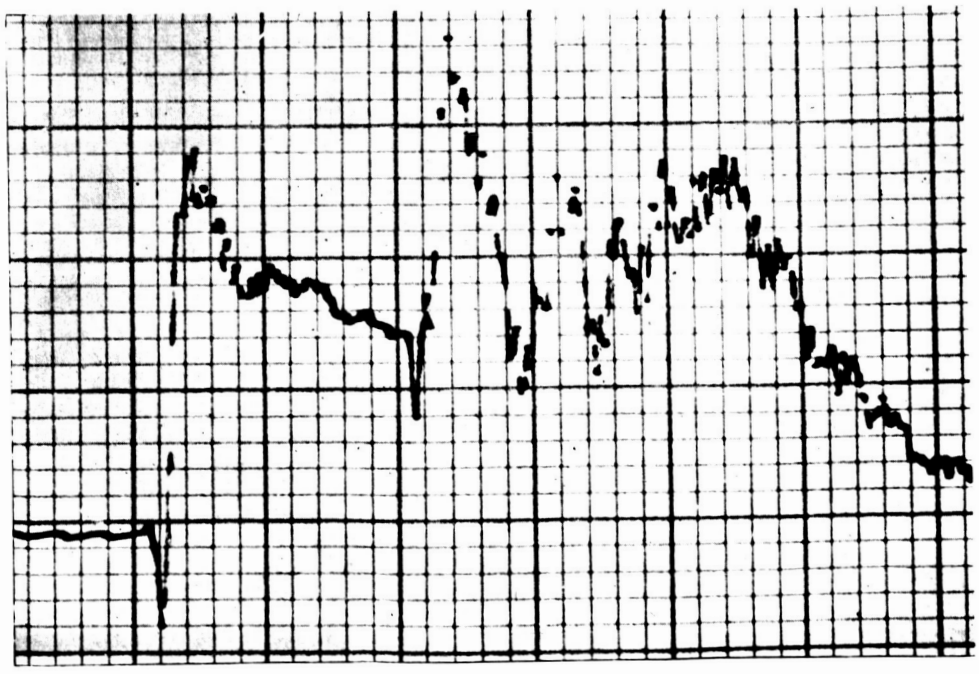

Figure No. 67. Response from Detector No. B, Run No. 5
Horizontal Scale Represents Time Increasing from Left to Right at 100 mm/sec.
Vertical Scale Is Voltage Output Set at 5 mv/mm.

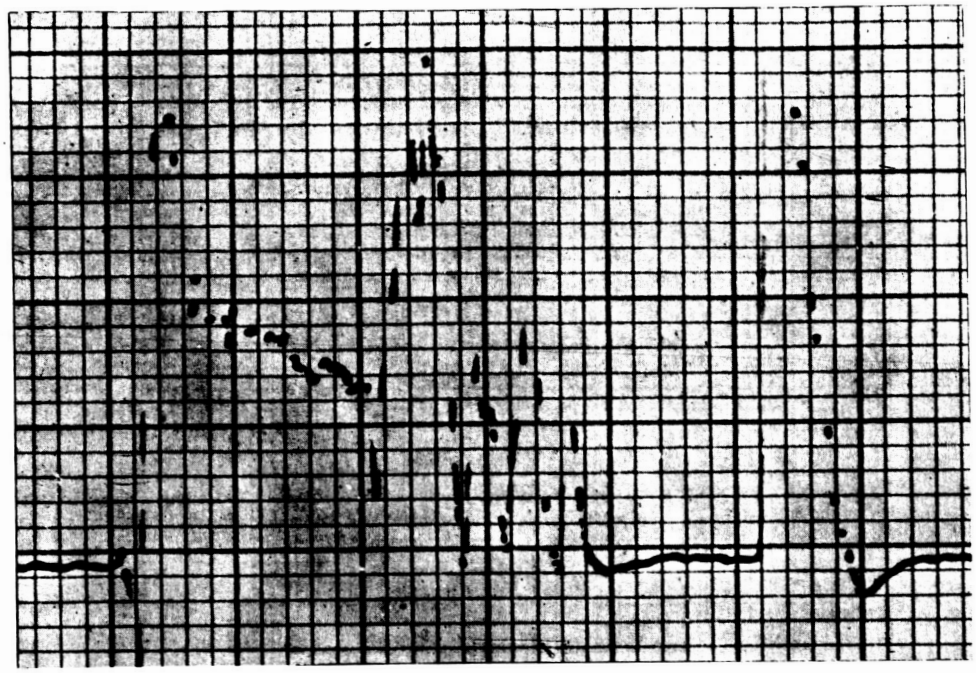

Figure No. 68. Response from Detector No. C, Run No. 5.
Horizontal Scale Represents Time Increasing from Left to Right at 100 mm/sec.
Vertical Scale Is Voltage Output Set at 5 mv/mm.

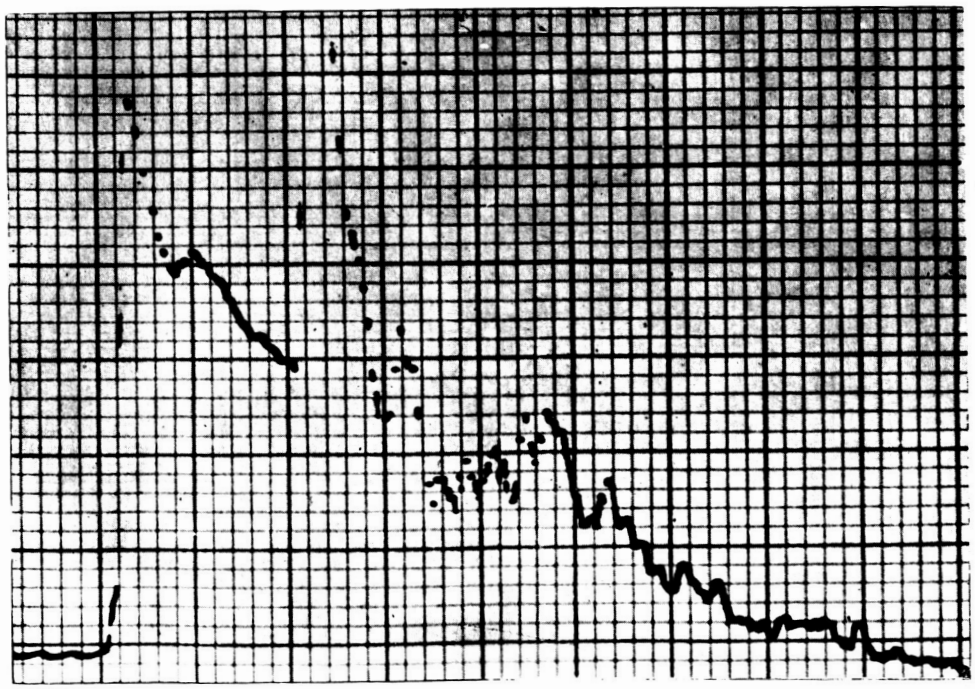

Figure No. 69. Response from Detector No. D, Run No. 5. 1301P
Horizontal Scale Represents Time Increasing from Left to Right at 100 mm/sec.
Vertical Scale Is Voltage Output Set at 5 mv/mm.

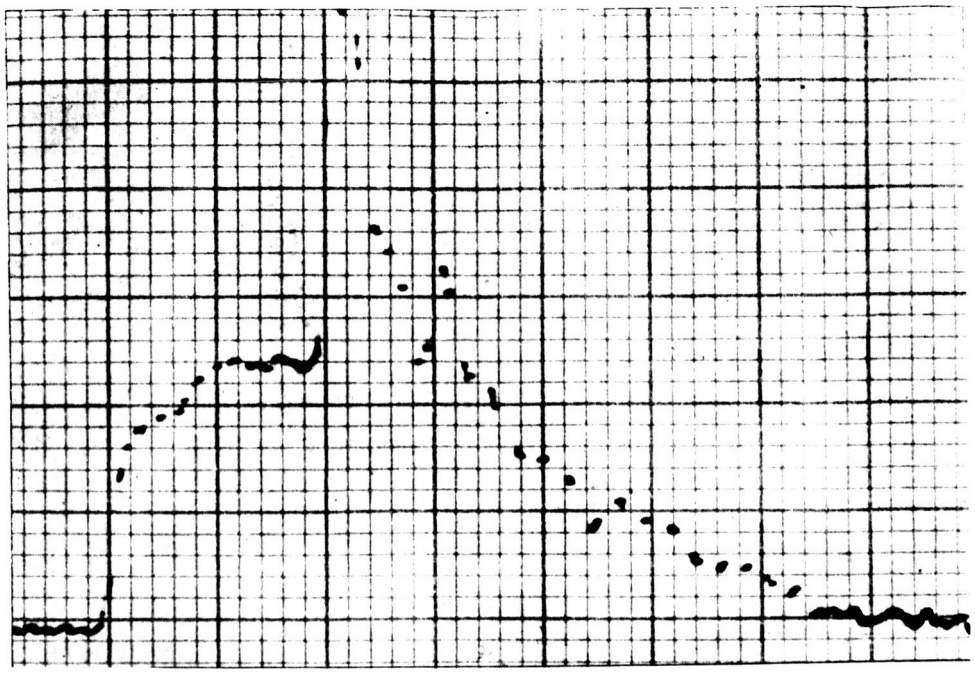

Figure No. 70. Response from Detector No. E, Run No. 5.
Horizontal Scale Represents Time Increasing from Left to Right at 100 mm/sec.
Vertical Scale Is Voltage Output Set at 5 mv/mm.

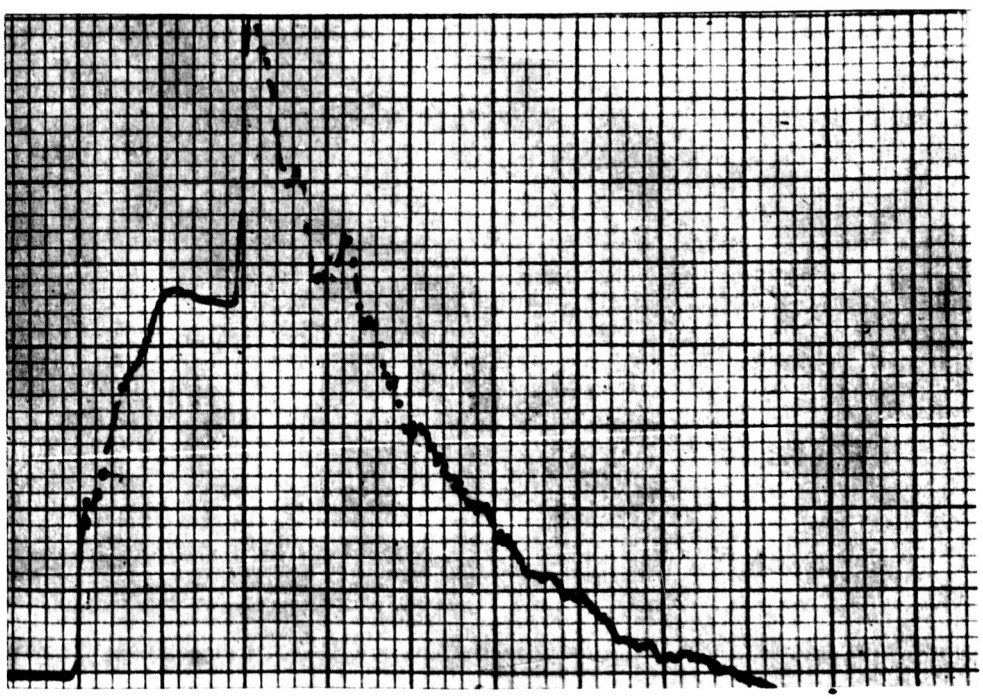

Figure No. 71. Response from Detector No. F, Run No. 5.
Horizontal Scale Represents Time Increasing from Left to Right at 100 mm/sec.
Vertical Scale Is Voltage Output Set at 5 mv/mm.

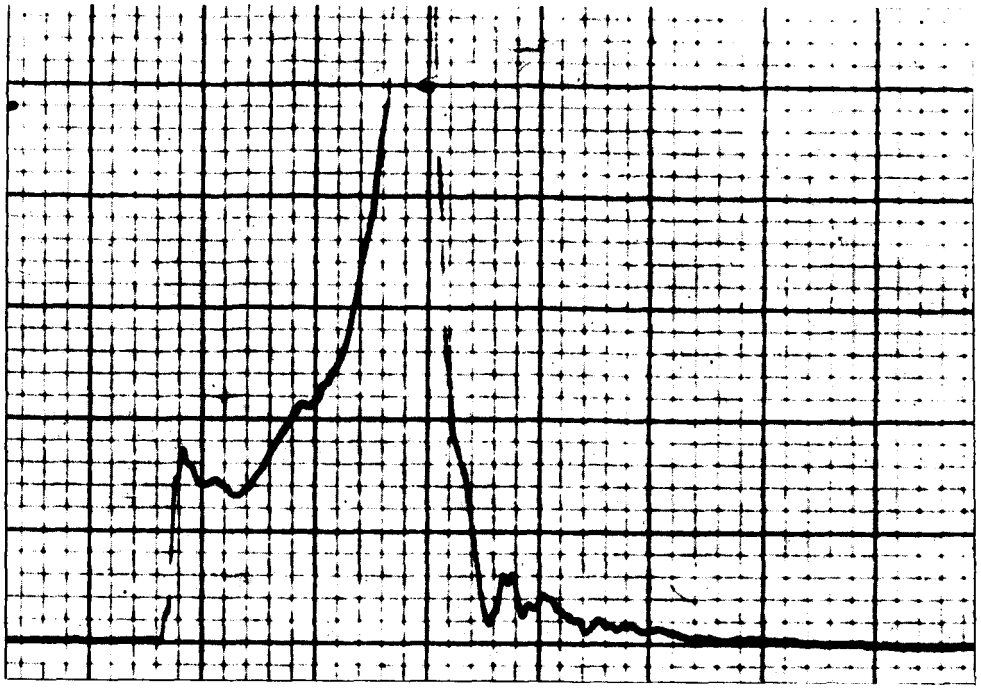

1290P

Figure 72. Response from Detector No. L, Run No. 5.
Horizontal Scale Represents Time Increasing from Left to Right at 100 mm/sec.
Vertical Scale Is Voltage Set at 1 v/cm

4.8 RESPONSE OF CERAMIC ELEMENTS VERSUS THICKNESS

Calibration of the detectors which had been constructed for the Langley effort showed a reproducibility in response from detector to detector not previously found in either single crystals or ceramic detectors. This showed promise as a means of comparing experimental and theoretical results. Since all the barium titanate was used for the Langley effort, a new order was processed for this purpose. The material was ordered from the Titanium Alloys Division of the National Lead Company. It was discovered that a higher grade material was available than had been previously used, so the higher grade was ordered. The higher grade "c.p." had only 0.07% impurities present, compared to the 2.65% present in the previously used Ticon B "p" grade. The firing temperature of the new material was somewhat different from the older material and the detectors made from the new material did not show quite the consistency of previous ones.

Figure 73 shows the capacitance of the detectors as a function of thickness. The circled points are the data from the detectors and the curve is proportional to 1/r as predicted. As can be readily seen, the data is in good agreement with this curve. A slight spreading is noticed for the thinner detectors. In regard to this spreading, the detectors were observed to have cavities in the surface roughly 1 or 2 mils deep. This occurred at all thicknesses. This effect would be expected to influence the thinner detectors more than the thicker ones because the holes become comparable to the dimensions of the detectors fro the thinner ones. Figure 74 shows the pyroelectric signal as a function of thickness. Here again the circled points show the experimental data and the curve is the theoretically predicted one. The disagreement at seven mils is attributed to the surface holes previously mentioned. The theoretical discussion for ceramic elements will be covered in the next section.

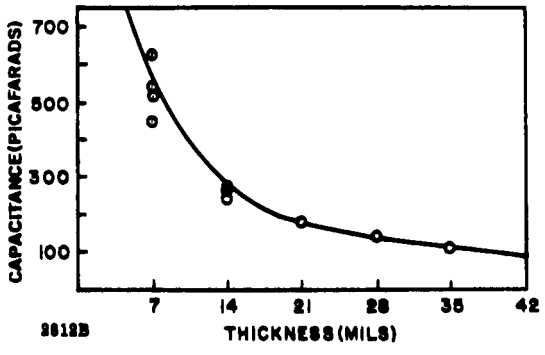

Figure 73. Capacitance of $BaTiO_3$ Ceramic Detectors as a Function of Thickness. The Circled Points Are the Experimental Data. The Curve Is the Theoretically Predicted Curve.

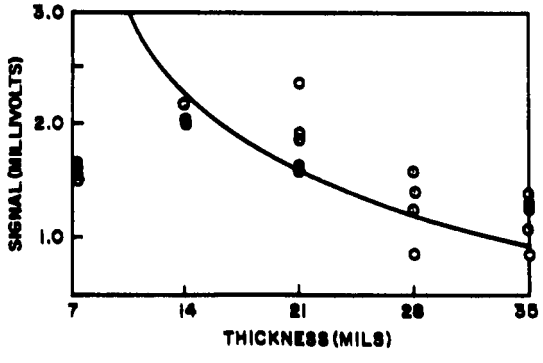

Figure 74. Pyroelectric Signal as a Function of Thickness. The Circled Points Are the Experimental Data. The Curve Is the Theoretically Predicted Curve.

4.9 THEORY

4.9.1 Review of Single Crystals

It was shown in the first phase of this contract that the equivalent circuit for pyroelectric materials being used was of the form depicted in Figure 75.

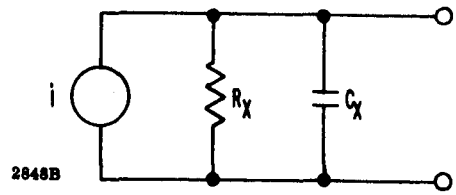

Figure 75. Equivalent Circuit for Pyroelectric Materials

In this figure the waveform of the ideal current generator is given by

$$i = A\frac{dP_s}{dt} = A\frac{dP_s}{dT}\frac{dT}{dt} \qquad (1)$$

where

R_x = resistance of pyroelectric element

C_x = capacitance of pyroelectric element

A = area of pyroelectric element

$\frac{dP_s}{dT}$ = pyroelectric coefficient

$\frac{dT}{dt}$ = time rate of change of temperature.

Before further analysis can be accomplished using this equivalent circuit, it is necessary to relate the time rate of change of the temperature to the incident energy to be detected. Thus, in the first phase, the approximation was made for single crystal elements that a fraction α of the incident energy would be absorbed by the element and this resulted (assuming a uniform volume distribution of this energy) in the following expression for the noise equivalent power (NEP) and specific detectivity (D*) - - from equation (17) of the Final Report for the first phase.

$$D^* \doteq \left[\frac{\frac{dP_s}{dT}}{\rho c_p\sqrt{\epsilon' \tan\delta}}\right]\left[\frac{\alpha}{4\sqrt{kT\ell\omega}}\right] \qquad (2)$$

$$NEP \doteq \frac{\rho c_p \sqrt{\epsilon' \tan\delta}}{\frac{dP_s}{dT}} \quad \frac{4\sqrt{kTA\ell\omega}}{\alpha} \tag{3}$$

In these equations

α	=	fraction of incident energy absorbed
$\frac{dP_s}{dT}$	=	pyroelectric coefficient
ρ	=	density of pyroelectric material
c_p	=	specific heat at constant pressure
ϵ'	=	real part of dielectric constant
tan	=	dielectric loss tangent
k	=	Boltzman's constant
A	=	area
ℓ	=	thickness
ω	=	angular frequency of modulation
T	=	absolute temperature

The desire, of course, is to make D* as large as possible or to make NEP as small as possible. The expression for these quantities has been written as two distinct factors in each case. The first factor involves only those quantities that depend on the bulk properties of the material used for the sensitive element whereas the second factor contains all remaining quantities. Consequently, the first factor in equation (2) should constitute a reasonable figure of merit (F) for pyroelectric materials. A figure of merit for pyroelectric is therefore defined as

$$F = (dP_s / dT) / (c_p \rho \sqrt{\epsilon' \tan\delta}). \tag{5}$$

The above approach gave valuable guidelines for the experimental work to follow and in particular suggested that achieving thin detector elements would be a fruitful means of improving achieved sensitivities. However, careful quantitative correlation between experimental and theoretical values of noise equivalent power (or detectivity) have been impossible using single crystals due to the detrimental effect of uncontrollable factors such as strain and other imperfections in the crystals. However, comparison of the best experimental values compared favorably with theoretical values.

4.9.2 Ceramic Elements

During the investigations of ceramic elements it was learned that they gave much greater reporducibility than single crystal elements. For this reason it was decided to compare theory and experiment for the ceramic elements. This decision requires a modification in the theoretical approach for the following reason.

The ceramic elements are opaque and it therefore follows that the incident energy absorbed by these elements will all be absorbed at the front face. Consequently the following boundary conditions are taken as being reasonable for the ceramic elements. All energy enters the element at the front face and no energy leaves the crystal in the time interval of interest. These boundary conditions give rise to the following boundary value problem. We consider a slab of material of thickness ℓ. (See Figure 76). Its front face is at $x = \ell$ and the back face at $x = 0$. Radiation of constant intensity I_0 is turned on at $t = 0$ and it is assumed the front face absorbs energy at the rate $\alpha I_0 A$ where A is the area of sample and α the fraction of intensity that is absorbed. Thus, it is desired to solve the heat equation.

$$\frac{\partial^2 T^*}{\partial x^2} = \frac{1}{K} \frac{\partial T^*}{\partial t} \qquad (6)$$

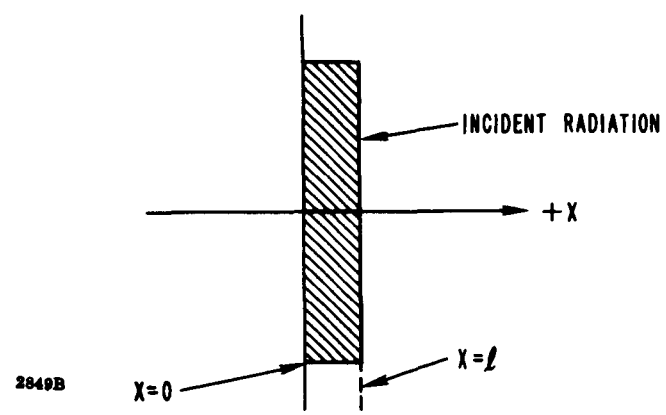

Figure 76. Illustration for Boundary Value Problem

subject to the conditions

$$k\frac{\partial T^*}{\partial x}\bigg|_{x=\ell} = \alpha I_o \tag{7}$$

$$k\frac{\partial T^*}{\partial x}\bigg|_{x=0} = 0 \tag{8}$$

and

$$T^*(x,t)\Big|_{t=0} = 0 \tag{9}$$

In the above equations $T^*(x,t)$ represents the temperature of the sample at position x and time t less the temperature of its environment which is assumed constant. The solution[9] to this problem can be written as follows

$$T^* = \frac{\alpha I_o t}{\rho c_p \ell} + \frac{\alpha I_o \ell}{k}\left\{\frac{3x^2-\ell^2}{6\ell^2} - \frac{2}{\pi^2}\sum_{n=1}^{\infty}\frac{(-1)^n}{n^2}\, e^{\frac{-kn^2\pi^2}{\ell^2}t}\cos\frac{m\pi x}{\ell}\right\} \tag{10}$$

From equation (10) it is seen that the space average temperature is

$$\langle T^*\rangle = \frac{1}{\ell}\int_0^{\ell} T^*(x,t)dx = \frac{\alpha I_o t}{\rho c_p \ell} \tag{11}$$

Therefore

$$\frac{d\langle T^*\rangle}{dt} = \frac{\alpha I_o}{\rho c_p \ell} \tag{12}$$

Consequently, from equation (1) it is seen that the ideal generator acts like a constant current generator if incident intensity is constant and if the assumed boundary conditions are met. Thus, from equations (1) and (12)

$$i = A\frac{dP_s}{dT}\frac{\alpha I_o}{\rho c_p \ell} \tag{13}$$

for I_o constant. This result can be used to compare theory and experiments.

---

[9] Carslaw, H.S. and J.C. Jaeger, Conduction of Heat in Solids, Oxford Press, p 112. (1959).

4.9.3 Loss Tangent

The measurement of dielectric loss tangent at low frequencies (15 cps in our case) having values larger than 0.10 is difficult with standard bridges. In view of this the following procedure was developed by this laboratory. At this writing it is not known whether the method has been reported in the literature by independent sources.

If a capacitor is made using the material whose loss tangent is desired as the dielectric it is well known that a finite loss tangent has the effect of altering the phase difference between the current through and voltage across the capacitor from the idealized 90 degrees. Thus, for sinusoidal source of angular frequency ω

$$I = j\omega CV \tag{14}$$

where I and V are the phasor current and phasor voltage respectively, C is the complex capacitance and j is the imaginary number such that $j^2 = -1$. If we choose the sample in the shape of a slab with cross-sectional area A and thickness ℓ, we can express C in terms of the complex dielectric constant as follows

$$C = \frac{A\epsilon}{\ell} = \frac{A\epsilon'}{\ell}(1 - j\tan\delta). \tag{15}$$

Here ϵ' is the real part of the dielectric constant and $\tan\delta$ is the loss tangent.

Thus

$$I = j\frac{\omega A\epsilon'}{\ell}(1 - j\tan\delta)V. \tag{16}$$

From equation (16) it follows that the current leads the voltage by an angle of

$$\theta = \frac{\pi}{2} - \delta \tag{17}$$

where θ is expressed in radians. Consequently its phase relative to an ideal capacitor is δ. We can use this fact in the following configuration which will allow a determination of $\tan\delta$. Consider the configuration as illustrated in Figure 77.

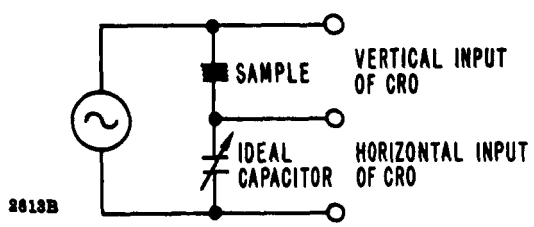

Figure 77. Circuit for Loss Tangent Measurements

The ideal capacitance is adjusted such that amplitude of the two signals are equal.

We can then express the vertical and horizontal deflections as

$$y = A \sin(\omega t + \delta) \qquad (18)$$
$$x = A \sin \omega t$$

From equation (18) it follows that

$$x^2 + y^2 - 2xy \cos \delta = \sin^2 \delta \qquad (19)$$

This is the equation of an elipse with its axes rotated 45° counterclockwise with respect to the CRO axes. The lengths of the semi-major axis, a, and semi-minor axis, b, are given by

$$a^2 = \frac{\sin^2 \delta}{1 - \cos \delta} \qquad (20)$$
$$b^2 = \frac{\sin^2 \delta}{1 + \cos \delta}$$

Let r = b/a, then from equation (20)

$$r^2 = \frac{1 - \cos \delta}{1 + \cos \delta} \qquad (21)$$

Solving equation (21) for $\tan \delta$ gives

$$\tan \delta = \frac{2r}{1 - r^2} \qquad (22)$$

The parameter r (= b/a) can be determined to within a few percent for r between about 0.02 and 1.0 thus loss tangents as small as 0.04 can be determined. If the accuracy of $\tan \delta$ is to be roughly the same as that for the measurement of r we must require

$$r < 1/\sqrt{3} \qquad (23)$$

which means that accurate loss tangent measurements are limited to values less than about 1.71 Thus, this procedure provides accurate loss tangent measurements at any frequency compatible with the CRO and satisfying

$$0.04 < \tan \Delta < 1.7 \qquad (24)$$

5. CONCLUSIONS AND RECOMMENDATIONS

The course of this program has been that of investigating various pyroelectric materials to determine their potential as pyroelectric detectors, to correlate known parameters of these bulk materials with the pyroelectric effect, to obtain a specific detectivity of 3×10^8 $(cps)^{1/2}$ cm/watt, and to determine the practicality of pyroelectric devices.

Several materials were evaluated both by measuring their pyroelectric response and by evaluating their figure of merit (discussed in Section 4.3). Barium titanate and tri-glycine sulfate were the best materials found. Tri-glycine sulfate is slightly better than barium titanate, although it is hygroscopic and more fragile. The hygroscopic nature of tri-glycine sulfate causes serious deterioration problems.

Since the theory predicted that the pyroelectric signal was inversely proportional to the thickness of the detector, strong consideration was given to means of producing thin detectors. Etching and lapping techniques successfully reduced thickness to approximately one mil; but strains and cracks greatly limited the successful application of these processes beyond that point.

Certain measurements were made on ceramic materials in order to compare experimental result with theoretical predictions. These measurements supported the inverse proportionality of pyroelectric response to thickness.

Efforts were made to grow single crystalline thin films of barium titanate and tri-glycine sulfate, but these efforts were only partially successful. Although films were grown which produced hysteresis loops, none showed a pyroelectric response. These results lead us to conclude that the difficulties involved in producing an efficient, single crystalline, thin film would be of sufficient magnitude to require a research program directed solely to this end. We would not recommend the inclusion of this problem in a more general research program; neither would we recommend that further efforts to reduce thickness be pursued without a thin film breakthrough.

The hot spot phenomenon was investigated and the hot spots were found to exist. The lack of time due to the extensive effort on the ceramic work and deterioration in the operation of the laser used in these studies permitted little to be concluded concerning the nature of these hot spots. We recommend that further research

work be solicited to determine the nature of these spots since we feel that this information would lead to a better understanding of the pyroelectric effect.

Ceramic detector elements were constructed for testing in the hot shot tunnel at Langley Research Center. This effort was initiated because existing means for the measurement of heat transfer were extremely tedious. They required several temperature measurements for each run with each thermocouple installed in the model, so that heat transfer equations yielding the power densities present could be solved with a computer. The data sampling system necessary for gathering this information was also quite complex.

Pyroelectric detectors would greatly simplify the measurement of these power densities. Since these detectors gave an output directly proportional to the incident power, one could read the power density directly at any time once this detector had been calibrated. The only equipment needed is a means of recording the output voltage.

Discussions revealed that an agreement of no better than a factor of 2 between thermocouples and pyroelectric detectors on initial tests would be reason for optimism concerning the use of these detectors in this capacity.

Personnel at Langley who were connected with these tests were extremely well pleased with the performance of these detectors. Mr. Pierce Lawing, who was in charge of the tunnel during these tests, expressed a strong desire to have these results published and to have the work continued.

We would recommend that ceramic elements with higher Curie temperatures be investigated, since this would make possible the measurement of a higher incident power. Improvement in readout systems is also recommended, since rise time could be greatly improved by widening the frequency response of the amplifiers.

We feel that the ceramic effort was a resounding success to the development extent of this program and NASA would benefit greatly by soliciting further work in this area.

"The aeronautical and space activities of the United States shall be conducted so as to contribute . . . to the expansion of human knowledge of phenomena in the atmosphere and space. The Administration shall provide for the widest practicable and appropriate dissemination of information concerning its activities and the results thereof."

—NATIONAL AERONAUTICS AND SPACE ACT OF 1958

NASA SCIENTIFIC AND TECHNICAL PUBLICATIONS

TECHNICAL REPORTS: Scientific and technical information considered important, complete, and a lasting contribution to existing knowledge.

TECHNICAL NOTES: Information less broad in scope but nevertheless of importance as a contribution to existing knowledge.

TECHNICAL MEMORANDUMS: Information receiving limited distribution because of preliminary data, security classification, or other reasons.

CONTRACTOR REPORTS: Technical information generated in connection with a NASA contract or grant and released under NASA auspices.

TECHNICAL TRANSLATIONS: Information published in a foreign language considered to merit NASA distribution in English.

TECHNICAL REPRINTS: Information derived from NASA activities and initially published in the form of journal articles.

SPECIAL PUBLICATIONS: Information derived from or of value to NASA activities but not necessarily reporting the results of individual NASA-programmed scientific efforts. Publications include conference proceedings, monographs, data compilations, handbooks, sourcebooks, and special bibliographies.

Details on the availability of these publications may be obtained from:

SCIENTIFIC AND TECHNICAL INFORMATION DIVISION

NATIONAL AERONAUTICS AND SPACE ADMINISTRATION

Washington, D.C. 20546